

**THE UNIVERSITY OF MICHIGAN
DEPARTMENT OF ATMOSPHERIC, OCEANIC, AND
SPACE SCIENCE**

**Space Physics Research Laboratory
2245 Hayward Street
Ann Arbor, Michigan 48109-2143**

*INTERIM
IN-91-CR
910
72 P*

Contract/Grant No.: NAGW-3585

Project Name: Studies for the Loss of Atomic and
Molecular Species from IO

Report Author(s): Michael R. Combi

Author(s) Phone: 313/764-7226

Report Preparation Date: 7 April 1994

Report Type: Annual Report

Period Covered: May 1, 1993 - April 30, 1994

Project Director:
Principal Investigator(s): Michael R. Combi

Program Technical Officer: Jay T. Bergstralh
Planetary Atmospheres Program
Office of Space Science and Applications
Code SLC
NASA HQ
Washington, DC 20546

(NASA-CR-195702) STUDIES FOR THE
LOSS OF ATOMIC AND MOLECULAR
SPECIES FROM IO Annual Report, 1
May 1993 - 30 Apr. 1994 (Michigan
Univ.) 72 p

N94-27941

Unclas

PROJECT DESCRIPTION

I. INTRODUCTION

The general objective of this project is to advance our theoretical understanding of Io's atmosphere and how various atomic and molecular species are lost from this atmosphere and are distributed in the circumplanetary environment of Jupiter. The proposal provides support for the activities of Michael Combi at the University of Michigan in collaboration with a larger project awarded to Atmospheric & Environmental Research, Inc., with primary principal investigator William H. Smyth. Michael Combi is the Principal Investigator and Project Manager for the Michigan grant NAGW-3585. This project provides for a continuation of a collaboration in similar efforts beginning in 1981, and with the object to apply theory to interpret and to relate a number of new and exciting observations for the atmospheric gases of the satellite. The ability to interpret and then to relate through the theoretical fabric a number of these otherwise independent observations is a central strength of this proposal. This comprehensive approach provides a collective power, extracting more from the sum of the parts and seeing beyond various limitations that are inherent in any one observation. Although the approach is designed to unify, the proposal is divided into well defined studies for the likely dominant atmospheric gases involving species of the SO₂ family (O, S, SO, O₂, SO₂) and for the trace atmospheric gas atomic sodium and a likely escaping molecular ion NaX⁺ (where NaX is the atmospheric molecule and X represents one or more atoms).

The relative abundance of the members of the SO₂ family and Na at the satellite exobase and their spatial distributions beyond in the extended corona of Io are not well known but will depend upon a number of factors including the upward transport rate of gases from below, the velocity distribution and corresponding escape rates of gases at the exobase, and the operative magnetospheric/solar-photon driven chemistry for the different gases. To date in the corona and near extended neutral clouds of Io, O and S have been observed in the UV emission lines over a number of years by IUE (Ballester et al. 1987; Ballester 1989; McGrath 1991), O has been detected in the optical (6300 Å) emission by ground-based observers (Schneider et al. 1989; Scherb and Roesler 1990; Brown 1991; Scherb 1991, 1992; Scherb and Smyth 1993). Na has been observed in the optical (5890 Å, 5896 Å) extensively for 20 years and most recently by Schneider et al. (1987), Schneider (1988 and 1991a). Although SO₂ has been observed in the local atmosphere of Io (Pearl et al. 1979; Lellouch et al. 1990, 1992), the angular extent of Io's surface covered by this gas and its vertical structure are still unknown. Observations of SO₂⁺ at ~5.3 Jupiter radii from the planet, and (most importantly) well inside Io's orbit (~5.9 RJ) by the Voyager 1 PLS instrument (Bagenal 1985) suggests that SO₂ is present at the exobase of Io with

the atomic species O, S and Na, and possibly other polyatomic species (NaX^+ ?), and may escape in large quantities despite its short 40-hour photodissociation lifetime and very short ~ 1 -hour electron impact dissociation lifetime in the plasma torus. The likely presence of molecules, or at least molecular ions, has further been suggested as a plausible mechanism to explain an unusually shaped fast sodium jet whose source is tied to the ion precursor species that is apparently locked into magnetic flux tubes in the corotating plasma torus (Schneider et al. 1991)

The scientific objectives of the larger collaborative program between AER, Inc. and the University of Michigan are to undertake theoretical modeling studies to simulate the distributions of the exospheric gases in Io's corona and extended clouds, to investigate the importance of the various physical processes that shape their relative abundances, and with these tools to analyze observations of O, S and Na obtained by three observers: M.A. McGrath of the Space Telescope Science Institute who has obtained Hubble Space Telescope observations of O and S near Io, F. Scherb who continues an effort to obtain 6300 Å OI observations as part of the University of Wisconsin Fabry-Perot program, and N.M. Schneider of the University of Colorado who obtained an extensive set of spectral and spatial observations of the Na emission near Io in the D-lines.

The major task for the University of Michigan portion of this work is the generalization of the Io sodium cloud model to simulate the ion-precursor of sodium that is the apparent source of the fast sodium jet observed by Schneider et al. (1991). The goal is a quantitative test of the molecular ion hypothesis with a model that is comparable to the general sodium cloud model published by us previously (Smyth and Combi 1988 a&b). A detailed comparison of observations with such a model will help to probe the feasibility of such a source and to examine the rates and scale lengths associated with the decay of the ion precursor so as to possibly uncover the identity of the parent ion. Another important task to be performed at Michigan is more supportive of AER in the general area of modeling the Na and SO_2 -family clouds.

II. PROGRESS DURING THE FIRST YEAR

During this first year, nearly completed work has concentrated on an analysis of a range of Io sodium observations, from the exobase of Io's corona (~ 700 surface above the surface) through the B-cloud (100 Io radii), in order to determine a consistent flux speed distribution of sodium moving upward in Io's atmosphere. In particular we have shown that a so-called modified sputtering distribution (or incomplete collisional cascade distribution) self-consistently reproduces entire set of Io sodium observations. A complete sodium source rate speed distribution at the satellite exobase, which includes the higher-speed (20-100 km/s) single elastic scattering and charge-exchange sources has also been suggested. The results of this effort have been written in a paper that has already been written and submitted for publication during this

project year in Icarus (Smyth and Combi 1994). A preprint of the paper appears attached as an appendix to this progress report.

Work scheduled to be completed by the end of this first project year, as outlined in our original proposal, includes beginning model development for the possible molecular-ion source for fast sodium in our zenocorona (or magneto-nebula) model (Smyth and Combi 1991), developed originally as an outgrowth of our comet coma model (Combi and Smyth 1988 a&b). Most of this effort has been delayed until the very end of the first project-year because of various commitments in other projects at AER.

III. PROGRAM OF WORK FOR THE SECOND YEAR

The major task for the University of Michigan portion of this joint project with AER, Inc., is to extend the work of Smyth and Combi (1991)--which explored the scenario of a direct source of high speed sodium from the exobase to explain the general structure of the zenocorona--in order to explore the physical formation of a distributed high speed source for sodium arising from an ion-precursor traveling along with the cororating plasma torus in the magnetosphere ahead of Io. Schneider et al. (1991) have suggested a plausible scenario for the ion-precursor to be the dissociative recombination of NaX^+ originally lost from Io's vicinity, and producing a stream of Na atoms on the scale of a few hours. The goal is to modify current models which produce Na atoms from Io's exobase, to first follow the ion precursors (e.g., NaX^+) as they travel down stream of Io in the plasma torus and oscillate up and down along magnetic flux tubes. A key part of this project is to folow the physical evolution which will be spatially variable in the plasma torus and to determine the physical characteristics of the distributed source that can produce the Na jet. The technique to be used in this generalization is exactly parallel with our earlier work for modeling the distribution of daughter and granddaughter species in the comae of comets (Combi and Smyth 1988 a&b). The model will be compared both with near-field images of the jet as well as any newly available images of the zenocorona (magneto-nebula). A supporting role to AER in the area of sodium and SO_2 -family cloud modeling will also be undertaken at the University of Michigan.

REFERENCES

- Bagenal, F. 1985. *J. Geophys. Res.* **90**, 311-324.
- Ballester, G.E. 1989. Ph.D. Thesis, The Johns Hopkins University.
- Ballester, G.E. H.W. Moos, P.D. Feldman, D.F. Strobel and M.E. Summers. 1987. *Astrophys. J.* **316**, L33-L38.
- Brown, M.E. 1991. *Bull. A.A.S.* **23**, 1134.
- Combi, M.R. and W.H. Smyth. 1988a. *Astrophys. J.* **327**, 1026-1043.
- Combi, M.R. and W.H. Smyth. 1988b. *Astrophys. J.* **327**, 1044-1059.
- Lellouch, E., M. Belton, I. dePater, S. Gulkis, and T. Encrenaz. 1990. *Nature* **346**, 639-641.
- Lellouch, E., M. Belton, I. dePater, G. Paubert, S. Gulkis, and T. Encrenaz. 1992. Preprint.
- McGrath, M.A. 1991. Private communication.
- Pearl, J., R. Hanel, V. Kunde, W. Maguire, K. Fox, S. Gupta, C. Ponnamperuma, and F. Raulin. 1979. *Nature* **280**, 755-758.
- Scherb, F. 1991. Private communication
- Scherb, F. and W.H. Smyth. 1993. *J. Geophys. Res.* **98**, 18729-18736.
- Scherb, F. and F. Roesler. 1990. Presented at "Magnetospheres of the Outer Planets: Fred Scarf Memorial Symposium", Annapolis, MD, August 20-24.
- Schneider, N.M. 1988. Ph.D. thesis, University of Arizona.
- Schneider, N.M., D.E. Shemansky, and K.C. Yu. 1989. *Bull. A.A.S.* **21**, 988-989.
- Schneider, N.M., D.M. Hunten, W.K. Wells, A.B. Schultz, and U. Fink. 1991. *Astrophys. J.* **368**, 298-315.
- Schneider, N.M., J.T. Trauger, J.K. Wilson, D.I. Brown, R.W. Evans and D.E. Shemansky. 1991. *Science* **253**, 1394-1397.
- Smyth, W.H. and M.R. Combi. 1988a. *Astrophys. J. Supp.* **66**, 397-411
- Smyth, W.H. and M.R. Combi. 1988b. *Astrophys. J.* **328**, 888-918.
- Smyth, W.H. and M.R. Combi. 1991. *J. Geophys. Res.* **96**, 22711-22727.
- Smyth, W.H. and M.R. Combi. 1994. Icarus (submitted). Also attached as an Appendix.

APPENDIX

Io's Sodium Corona and Spatially Extended Cloud: A Consistent Flux Speed Distribution. W.H. Smyth and M.R. Combi. *Icarus* (submitted)

Io's Sodium Corona and Spatially Extended Cloud :

A Consistent Flux Speed Distribution

William H. Smyth¹

Michael R. Combi²

Submitted to Icarus

October 29, 1993

1. Atmospheric and Environmental Research, Inc., Cambridge, MA 02139
2. Space Physics Research Laboratory, University of Michigan, Ann Arbor, Michigan 48109

Number of manuscript pages : 46

Number of Figures : 16

Number of Tables : 5

Key words : Io, satellite exospheres, gas tori

Running heading : Io's Sodium Corona and Spatially Extended Cloud

For editorial correspondence and proofs please contact:

William H. Smyth

Atmospheric and Environmental Research, Inc.

840 Memorial Drive

Cambridge, MA 02139

Telephone number : (617) 547-6207

Fax number : (617) 661-6479

Internet : smyth@aer.com

ABSTRACT

A data set, composed of different ground-based observations for Io's sodium corona and spatially extended sodium cloud and covering the spatial range from Io's nominal exobase of 1.4 satellite radii to east-west distances from Io of ± 100 satellite radii, is analyzed collectively to investigate the velocity distribution of sodium at the exobase. The data set is composed of the novel 1985 eclipse measurements of Schneider *et al.* (1991) acquired from 1.4 to ~ 10 satellite radii from Io, the 1985 east-west emission data of Schneider *et al.* (1991) acquired from ~ 4 to ~ 40 satellite radii from Io, and sodium cloud image data acquired from ~ 10 to ~ 100 satellite radii from Io by a number of different observers in the 1976 to 1983 time frame. The column density distributions determined from the different eclipse measurements are essentially symmetric about Io within the Lagrange sphere radius (5.85 satellite radii, i.e., the gravitational grasp of the satellite), providing an one-dimensional radial profile as noted earlier by Schneider *et al.* (1991). At distances beyond the Lagrange sphere radius, however, the apparent change in the observed column density slope is shown in model calculations to occur in the forward cloud, but not trailing cloud portion, of the column density profile. The east-west sodium brightness profiles as determined from the emission data are distinctly different in front of Io and behind Io and are shown to exhibit the time-dependent behaviors of the forward cloud and the trailing north-south oscillating directional features, which are correlated with the Io geocentric phase angle, the Io System III longitude, and the east-west asymmetry of the plasma torus. In this regard and of particular interest, an observed brightness enhancement of the trailing cloud portion of the east-west emission data profile, which is also correlated with an observed enhancement in the full width half maximum of the measured spectral line shape, is identified as occurring when the (higher-speed) trailing directional feature crossed the east-west position of the observing slit (i.e., the null position

between north and south). The combined data set is analyzed using the sodium cloud model of Smyth and Combi (1988a,b). At the satellite exobase, the speed dispersion of either an isotropic Maxwell-Boltzmann flux speed distribution or an isotropic classical sputtering flux speed distribution (which has a broader dispersion) is shown to be inadequate in fitting the combined data set. In the absence of the trailing cloud enhancement at the null condition, an isotropic modified sputtering flux speed distribution provides an excellent fit to the combined data set for a sodium source of 1.7×10^{26} atoms sec^{-1} . To fit also the enhanced trailing cloud profile at the null condition, an additional enhanced high-speed ($\sim 15\text{-}20 \text{ km sec}^{-1}$) sodium population is required which is nonisotropically ejected from the satellite exobase so as to preferentially populate the trailing cloud rather than the forward cloud. Such a nonisotropic high-speed population of sodium is consistent with the earlier modeling analysis of the directional features by Pilcher *et al.* (1984). A complete sodium source rate speed distribution function at the satellite exobase, which also includes the even higher-speed ($\sim 20\text{-}100 \text{ km sec}^{-1}$) charge-exchange source (Smyth and Combi 1991) at Io that populates the sodium zenocorona (or magnetonebula) far from Jupiter, is presented.

1. INTRODUCTION

Novel ground-based observations of Io's sodium corona and near extended cloud were obtained in 1985 by Schneider (1988; Schneider *et al.* 1987, 1991) when the Galilean satellites of Jupiter underwent mutual eclipse. These observations provide for the first time valuable information about the density gradient of atomic sodium within the Lagrange sphere of Io (i.e., a radius of 5.85 satellite radii, R_{Io}) and also provide spatial information beyond this boundary that extends into the nearer portion (i.e., 6-40 R_{Io} from Io's center) of the sodium cloud. Two different types of observations were acquired: eclipse observations and emission observations. Eclipse observations measured the absorption feature at the D-line wavelengths as seen from Earth in the spectra of the reflected sunlight from the disk of another Galilean satellite (either Europa or Ganymede for measurements of interest here) that was produced by sodium in Io's atmosphere as Io eclipsed the sun from the viewpoint of the other Galilean satellite. Since the equivalent width of each absorption profile can be directly converted to a column abundance of sodium along the optical path, successive measurements during one solar eclipse of either Europa or Ganymede by Io produce a spatial profile of the column density near Io. Emission observations measured the solar resonance scattered D-line intensity emitted by sodium atoms in the near cloud environment of Io. In addition to spectral information, which will be only briefly considered here, these observations provide a one-dimensional spatial profile of the D-line emission brightnesses along a slit that is oriented east-west (i.e., perpendicular to the spin axis of Jupiter) and that contains (or very nearly contains) Io's disk. Eclipse data yield the most accurate information very near Io (i.e., 1.4 to 6 R_{Io} from Io's center), while emission

data yield the most accurate information at larger distances (i.e., 4 to 40 R_{Io}) as discussed in detail by Schneider *et al.* (1991).

In this paper, the spatial sodium profiles acquired in the 1985 eclipse and emission data are analyzed together with more spatially-extended east-west profiles extracted from earlier sodium cloud image observations in order to investigate the nature of the flux speed distribution of sodium atoms at Io exobase. The observational information is presented, compared, and evaluated in section 2. Modeling of the spatial profiles of the sodium data is undertaken in section 3. Discussion and conclusions are presented in section 4.

2. OBSERVATIONS

Of particular interest in this paper are the five higher quality eclipse measurements and the nine higher quality emission observations obtained at the Catalina Observatory 1.5 meter telescope using the LPL echelle spectrograph that were presented by Schneider *et al.* (1991). The dates, times, orbital angular parameters of Io, spectral ID numbers, and the numbering of these observations adopted in this paper are summarized in Table 1. Four of the five eclipse observations were acquired when Io was east of Jupiter (i.e., an Io geocentric phase angle within 90 ± 90 degrees), and only one was acquired when Io was west of Jupiter (i.e., within 270 ± 90 degrees). Seven of the emission observations were obtained when Io was east of Jupiter, and only two were obtained when Io was west of Jupiter. In addition, select sodium cloud image observations for Io near its orbital elongation points, which were acquired in 1976 by Murcray (1978; Murcray and Goody 1978), in 1981 by Goldberg *et al.* (1984; Goldberg and Smyth 1993), and in 1983 by Morgan (1984, private communication), are used to extract east-west D₂ brightness profiles that overlap the spatial range of the emission data and extend it to $\pm 100 R_{Io}$.

2.1 Eclipse Observations

The column density profiles for all five of the eclipse observations are presented collectively in Figure 1 and follow directly from the information given by Schneider *et al.* (1991) in their Table 3. Only one lower-bound data point from eclipse 4 at a distance from the center of Io of $1.17 R_{Io}$ is excluded since it is well within the nominally exobase radius of $1.4 R_{Io}$. The spatial profile for eclipse 2 obtained on September when Io was very near eastern elongation (i.e., 90 degrees Io phase angle) is highlighted in Figure 1 and seen to be similar to the other four spatial profiles. A comparison of the two sides of each eclipse measurement shows no detectable difference in the slopes of their separate profiles within the Lagrange sphere radius of Io. This was noted earlier by Schneider *et al.* (1991) and thus effectively reduces the eclipse data to a radially symmetric profile. The dashed line shows the power law fit to the data points contained within the Lagrange radius and has the form

$$N (1.4 \leq r \leq 5.85) = 2.55 \times 10^{12} r^{-2.48}$$

where N is the column density in units of atoms cm^{-2} and r is the distance from the center of Io in units of the R_{Io} (i.e., 1815 km). This is the same power law obtained earlier by Schneider *et al.* and undercuts the data points outside the Lagrange radius where the eclipse observations are deemed to be less reliable. Although the eclipse data beyond the Lagrange sphere contain more vertical scatter, they also appear to have possibly a reduced slope. Such a change in slope might be caused by the domination of the planetary gravitational field beyond the Lagrange radius of Io and will be discussed further in the modeling analysis section.

2.2 Emission Observations

The D₂ brightness profiles for the nine emission observations are shown collectively in Figure 2. This information, which was previously published only in a graphical format (Schneider *et al.* 1991), is summarized numerically in Table 2 as provided by Schneider (1990, private communication). The spatial profile for Emission 4, which was obtained on September 14 when Io was nearest eastern elongation, is highlighted, and its east and west profiles are identified separately. Excluding all data points inside of 4 R_{Io} where the seeing and instrumental effects artificially flatten the profile, the power law fit to the remaining emission brightness data in Figure 2 is given by

$$I_{D_2}(r \geq 4) = 101 r^{-1.45}$$

where I_{D_2} is the D₂ brightness in kiloRayleighs (kR) and r is the distance from the center of Io in R_{Io} units. This D₂ brightness of ~ 100 kR as r approaches Io's surface is consistent (Brown and Yung 1976) with the maximum sodium column density of ~1 x 10¹² atoms cm⁻² deduced from the eclipse data in Figure 1.

For more insight into the emission data, it is instructive to make a direct comparison of the relative behavior of the nine emission observations. Since the spatial coverage of the D₂ brightness is very nonuniform, this comparison can be readily accomplished by simply inspecting the columns in Table 2. The nonuniform spatial coverage in Table 2 occurs because of different distance intervals adopted to obtain an average brightness value (given different signal to noise ratios) for each data point in the profile and because of signal drop-out associated with constraints imposed on positioning the slit profile on the CCD detector

during interleaved eclipse and emission measurements. Using the emission data for Io east of Jupiter (i.e., seven out of the nine emission observations) and for Io west of Jupiter (i.e., the remaining two emission observations), the relative brightness of the forward and trailing sodium cloud near Io may be monitored as a function of the Io geocentric phase angle by comparing in each observation the two brightness profiles east and west of Io. In this comparison, it will be seen that systematic changes in the D₂ brightness are generally consistent with the Io phase angle dependence observed in Io sodium cloud image data over the last two decades.

When Io is east of Jupiter and has a phase angles less than about 65 degrees, a brighter forward sodium cloud is observed to the east of Io and a dimmer trailing cloud is observed to the west of Io (Goldberg *et al.* 1984). This is the pattern exhibited by the emission 1 observation on August 27 which has an average Io phase angle of 61.4 degrees.

When Io is east of Jupiter and has phase angle between about 65 and 85 to 90 degrees, east and west profiles are observed (Goldberg *et al.* 1984) to be very similar since the brighter forward sodium cloud is now swinging through and approximately aligned along the observer's line of sight. This is the pattern exhibited by the emission 2 observation on August 27 which has an average Io phase angle of 72.2 degrees. For the emission 4 observation acquired 18 days later on September 14 for an average Io phase angle of 87.7 degrees, the reverse pattern, however, is present with the trailing cloud being brighter than the forward cloud. Inspection of the line profile shapes for each data point of the emission 4 observation on September 14 indicates that its full width half maximum (FWHM) is highly asymmetric east and west of Io with a much larger FWHM present at larger distances from Io in the east profile (i.e., in the trailing cloud). The emission 3 observation acquired a day earlier for Io west of Jupiter (and essentially a mirror

geometric observation to that on September 14) and the emission 6 observation acquired for Io west of Jupiter a day later on September 15, also both exhibit a similar highly asymmetric values for the FWHM which are larger in the trailing cloud. This reversal of the normal pattern by the emission 3, the emission 4, and the emission 6 observations therefore all occur when additional high speed sodium was present in the trailing portion of the cloud outside of Io's orbit. The Doppler signature of this additional high speed sodium was, however, not seen in the trailing portion of the cloud in the emission 5 observation which was also acquired on September 14 only about one and one-half hours after the emission 4 observation (i.e., an increase in the Io phase angle and hence the cloud's sky-plane projection angle of only about 13 degrees).

When Io is east of Jupiter and has a phase angle greater than about 85 to 90 degrees, the forward sodium cloud is observed in image data to be brighter to the west of Io and the trailing cloud to be dimmer and to the east of Io (Goldberg *et al.* 1984). This is the pattern exhibited by the emission 7, emission 8, and emission 9 observations which have average Io phase angle of about 117, 122, and 143 degrees, respectively. A comparison of the forward and trailing cloud profiles for the emission 5 observation, which has an average Io phase angle of about 101 degrees, is not possible because there is only one data point west of Io.

When Io is west of Jupiter and has a phase angle greater than about 235 degrees, the forward sodium cloud is generally observed to be brighter and to the east of Io, and the trailing cloud is generally observed to be dimmer and to the west of Io (Goldberg *et al.* 1984). Examination of the profiles for the two out of the nine emission observations for Io west of Jupiter (i.e., emission 3 and emission 6 with Io phase angles of about 277 and 295 degrees, respectively), shows, however, the reverse pattern. As noted above, these two

observations, together with the eastern emission 4 observation, all exhibit this reverse pattern and also have a highly asymmetric spatial profiles east and west of Io for their FWHM values, with much larger FWHM values present at larger distances from Io in the trailing cloud . These asymmetric spatial profiles of the FWHM suggest additional high speed sodium in the cloud outside of Io's orbit may be responsible for this reverse pattern.

A final comparison in Table 2 can be made for the nearly mirror geometric measurements for the emission 7 observation with an Io phase angle of about 117 degrees and the emission 6 observation with an Io phase angle of about 295 degrees. From Table 2, the brightness of the forward cloud at a distance of 10-16 R_{Io} can be seen to be larger for Io east of Jupiter. This is consistent with the well known east-west intensity asymmetry first discovered near Io by Bergstralh *et al.*(1975, 1977) and identified at larger distances from Io by Goldberg and Smyth (1993). A similar comparison between the approximately mirror geometric measurements for the emission 4 observation with an Io phase angle of about 88 degrees and the emission 3 observation with an Io phase angle of about 277 degrees has not been considered since the absolute calibration of the emission 3 observation is in question (Schneider 1990, private communication).

A closer graphical examination of each of the nine profiles in Figure 2 shows that the vertical spread of the whole data set, particularly for $r > 10$, is a result of the superposition of the separate emission observations, where for each observation the slit profiles east and west of Io have two well defined but generally different slopes and different absolute brightnesses. This can readily be shown by a power-law fit analysis [$I_{D_i}(r \geq 4) = A r^{-\beta}$] of the separate east and west profiles for each emission observation for Io east of Jupiter, where the exponent, β , and amplitude, A , are summarized in Table 3. These fits omit data points inside four satellite radii of Io's center, where they are

artificially flattened, and thus depict the decay in the brightness profile primarily outside of the Lagrange radius. In Table 3, the emission observations are arranged in increasing Io phase angle, and the spatially-projected location of the forward cloud (F), the symmetric turning point (S) of the cloud, and the trailing cloud (T) are identified for the east and west profiles. The power law slopes of all the forward clouds are similar and have an exponent value of ~ 1.6 . The power law slopes of the trailing clouds after the symmetric turning point, excluding the September 14 emission observation at a phase angle of 100.6 degrees, are also similar and have an exponent value of ~ 2.0 . The power law slopes of the clouds at the symmetric turning point, excluding the September 14 emission observation of the trailing cloud at a phase angle of 87.7 degrees, are similar and have an exponent value of ~ 1.8 . The two power law slopes of the trailing clouds on September 14 do not follow the pattern and have smaller exponent values of ~ 1.23 and 1.27 . Not including the two emission observations on August 27 for Io east of Jupiter, which are at or before the symmetric turning point and have the reverse east-west projection orientation for their forward and trailing clouds, the remaining five profiles for Io east of Jupiter are presented graphically in Figure 3 along with their power law fits.

The brightness profiles for the forward cloud (i.e. west of Io) in Figure 3 are very tightly confined. The brightness profiles for the trailing cloud (i.e., east of Io) in Figure 3, however, are significantly different and drop off more rapidly with increasing Io phase angle. The brightest (i.e., least steep) of these profiles is for the emission 4 observation (87.7 degrees Io phase angle) that exhibited a much larger FWHM value in the trailing cloud for the data points at these larger distances from Io. The next brightest profile is for the emission 5 observation (100.6 degrees Io phase angle) acquired ~ 1.5 hours later on the same day which does not show the asymmetry in the FWHM values. The remaining three rather tightly confined trailing cloud profiles in Figure 3 are for the emission 7, emission 8,

and emission 9 observations that have a very similar slope of $\beta \sim 2$ as noted earlier. This behavior of the trailing clouds suggests that both the presence of higher speed sodium atoms as well as rapidly changing projection effects of the cloud on the sky plane as the Io phase angle increases are likely involved in its explanation. This behavior will be examined further and explained in the next section. In contrast, the well confined behavior of the forward sodium cloud and the absence of high speed sodium atom signatures suggest that the forward cloud is, as expected, primarily associated with the escape of low speed sodium from Io. A comparison of the brightness profiles in Figure 3 with other observations of the sodium cloud is undertaken below.

2.3 Sodium Cloud Image Observations

A large number of sodium cloud images in the D_1 and D_2 emission lines were acquired in the 1975-1984 time interval (Murcray 1978; Murcray and Goody 1978; Matson *et al.* 1978; Goldberg *et al.* 1980, 1984; Morgan 1984, private communication; Goldberg and Smyth 1993) where Io was centered behind an occulting mask typically 10 to 12 arc sec across (i.e., covering a radial distance from the center of Io of about $10 R_{Io}$) in order to block the bright disk-reflected sunlight from the satellite. Brightnesses in the immediate vicinity of the mask were usually spatially distorted in the resulting image but were consistently measured to be a few kiloRayleigh (kR). These brightness are similar to those of the emission data at $10 R_{Io}$ in Figure 2.

A simple review of these sodium cloud images shows that the forward sodium cloud is generally more spatially extended and brighter than the trailing cloud. An exception to this occurs, however, when the high-speed trailing directional-feature, which oscillates north and south behind the satellite with its inclination correlated (Pilcher *et al.*

1984) with the System III longitude angle of Io, passes through the east-west line drawn through Io (i.e., the null location of the directional feature). The observed correlations of the north inclination, the south inclination, and the null locations of the directional feature with the System III longitude of Io are shown in Figure 4 as determined by Goldberg and Smyth (1993) and are consistent with those obtained earlier by Pilcher *et al.* (1984). The directional feature changes from a south to north inclination for a null System III longitude angle of Io near 165 degrees and change from north to south for a rather poorly defined null System III longitude angle of Io somewhere between about 320 and 25 degrees. This changing north-south orientation of the trailing directional feature is illustrated in Figure 5 by three sodium cloud images, where an east-west oriented scale centered on Io of length $\pm 100 R_{Io}$ is shown for reference. In Figure 5, a north directional feature is present in image A (247 degrees Io System III longitude), a south directional feature is present in image B (104 degrees Io System III longitude), and a slightly north but near-null directional feature is present in image C (178 degrees Io System III longitude). The spatial extension and brightening of the trailing cloud profile along the east-west oriented (dashed) line, when the directional feature is near the null location, are readily apparent.

The forward cloud has been observed in images to distances of 100 satellite radii and more ahead of Io, where the cloud brightness levels are then only a few hundred Rayleighs. Analysis of the D_2 images of Murcray (1978) by Smyth and McElroy (1978 see their Fig. 4) indicated that when Io was near eastern elongation the one kR brightness level in the forward cloud occurred about $60 R_{Io}$ ahead of Io. Examination of a number of additional images indicates that the observed brightnesses of the forward cloud at this distance appear many times to be lower, although generally it has been difficult to be precise because the cloud is usually not measured to brightnesses less than about 0.2 to 0.5 kR. Using fourteen images of the sodium cloud for Io near its orbital elongation points that

are summarized in Table 4, a range (or an bounding envelope) of values for the D_2 east-west brightness profile of the forward and trailing clouds has been determined and is shown in Figure 3 by different shaded area.

For the forward cloud profile in Figure 3, the shaded area determined from the sodium cloud images occurs for radial distances greater than about $20 R_{Io}$ and can be seen to be brighter and to have a less steep slope than the emission data profiles. The lower boundary of the forward sodium cloud image profile area intersects the emission data just inside of $10 R_{Io}$, which is near the Lagrange radius of Io and is where the slope of the eclipse data in Figure 1 appears to become less steep. For Io near the elongation point, only two emission profiles occur and are too short to overlap the sodium cloud image data, with the one for an Io phase angle of 87.7 degrees extending only to a radial distance of $\sim 10 R_{Io}$ and the other for an Io phase angle of 100.6 degrees containing only one point at a radial distance of $\sim 15 R_{Io}$. For Io somewhat beyond eastern elongation, the remaining three emission data profiles (i.e., for Io phase angles of 117.2, 121.6, and 143.1 degrees) extend radially to $\sim 30 R_{Io}$ and fall below the sodium cloud image profile area, which is more representative of conditions near elongation. For Io near elongation, the question of consistency of the forward cloud brightness profiles from the emission data and the sodium cloud image data will be addressed in the modeling analysis section.

For the trailing cloud profile in Figure 3, two different shaded areas have been extracted from the sodium cloud image information in Table 4 to quantify its D_2 east-west brightness profile. The extracted profile areas represent the two basic orientations for the directional feature: (1) when the directional feature is either north or south (lower area) and (2) when the directional feature is at the null or near null location (upper area). These two areas establish a range (or an bounding envelope) for the values of the D_2 east-west

brightness profile of the trailing sodium cloud for Io near its orbital elongation point. As expected, the shaded area for the directional feature at the null location is both brighter and less steep than the shaded area for the directional feature with either a north or south inclination. As noted in Figure 5, the D₂ east-west brightness profile of the trailing sodium cloud is more closely confined to Io than the forward cloud when the trailing directional feature is inclined either north or south and has a less steep brightness gradient when the directional feature is at the null location.

The Io System III longitude correlated inclination of the directional feature is thought to be produced by high speed ($\sim 15\text{-}20 \text{ km sec}^{-1}$) sodium atoms escaping from Io in a nonisotropic manner. From the analysis of Pilcher *et al.* (1984), the nonisotropic escape flux is diminished at the poles relative to the equator and is also diminished in the forward and backward directions of the satellite's motion in comparison to the perpendicular direction of motion to Io's orbit in the satellite orbit plane. For these high speed sodium atoms, the Io System III longitude correlation is produced because atom trajectories, upon reaching the spatial region behind Io, are synchronized in such a way with the time-dependent sodium electron impact ionization sink of the oscillating plasma torus, so as to either go under it, go through it, or go over it, thereby producing an alternating north-south reduction in the sodium density.

In comparing the trailing emission profiles in Figure 3 with the trailing sodium cloud image data, it is important to identify the orientation of the directional feature in the emission data as classified by Figure 4 and also to note if there were enhancements in the measured Doppler signature of the trailing D₂ east-west brightness profiles. This information is summarized in Table 5. For the three emission profiles where an enhanced Doppler spectral profile (i.e., FWHM) was measured, the directional feature was at a null

or near null location, and also the trailing D₂ east-west brightness spatial profile was either similar or dominant (i.e., brighter and less steep) when compared to the forward cloud spatial profile. Two of these emission profiles occurred when Io was west of Jupiter and are not included in Figure 3. The third profile occurred for Io at a phase angle of 87.7 degrees. This is the brightest and least steep of all the profiles in Figure 3 and has a power law fit that is along the top boundary of the upper area for the sodium cloud image data which corresponds to the null condition. The presence of this brightest trailing profile is thus explained as a case where the directional feature was at a null condition. In Figure 3, the trailing emission profile for an Io phase angle of 100.6 degrees, acquired only about 1.5 hours later on the same night and having a south inclined directional feature, has a power law fit that is essentially along the top boundary of the lower area for sodium cloud image data which corresponds to a north or south inclined directional features. The remaining three emission profiles (i.e., for Io phase angles of 117.2, 121.6, and 143.1 degrees) are for Io somewhat beyond eastern elongation and lie near or just below the lower boundary of the lower area for sodium cloud images. The trailing emission profile data are therefore quite consistent with the sodium trailing cloud image data.

3. ANALYSIS OF THE OBSERVATIONS

Modeling analysis of the one-dimensional sodium distribution described in the previous section by the eclipse data, the emission data, and the sodium cloud image data will now be undertaken. One-dimensional profiles are calculated using the numerical sodium cloud model of Smyth and Combi (1988 a,b), where the electron impact ionization sink for sodium is determined for a 7 degree tilted corotating plasma torus with an offset-dipole planetary magnetic field in the presence of a nominal (i.e., $\sim 2.8 \text{ mV m}^{-1}$ in Io's frame) east-west electric field. Preliminary modeling reported earlier by Smyth and Combi

(1987) for the first radial profile published by Schneider *et al.* (1987) for the sodium column density determined by two eclipse measurements showed that it could be fit very well from ~ 4 to $10 R_{Io}$ by adopting a escaping, monoenergetic (2.6 km sec^{-1}), and isotropic sodium flux from the satellite exobase (assumed $1.4 R_{Io}$, where the escape speed is $\sim 2 \text{ km sec}^{-1}$), which was determined independently from modeling typical forward cloud image data in the D_2 emission brightness range of $\sim 1\text{-}3 \text{ kR}$. A similar conclusion is reached from a comparison in Figure 6 of this monoenergetic model run with the complete set of eclipse data from Figure 1. In the radial interval from ~ 2 to $15 R_{Io}$, the effect of the sodium lifetime on the calculated profile for this monoenergetic source is illustrated in Figure 7, where it is seen to alter primarily the absolute magnitude rather than the slope of the column density profile. To fit in addition the eclipse data in Figure 6 between the nominal exobase ($1.4 R_{Io}$) and $\sim 4 R_{Io}$, a properly chosen dispersion of initial velocities for the source flux distribution with non-escaping components is required. For the larger spatial distances beyond the Lagrange radius, covered by the east-west profiles for the emission data and the sodium cloud image data, the dispersion of initial velocities in the source for speed components greater than 2.6 km sec^{-1} may also need to be included. Indeed, the eclipse measurements for the corona near Io, the emission measurements that extend into the near sodium cloud, and the sodium cloud image derived profiles that reach to distances of $\pm 100 R_{Io}$, provide a set of spatially overlapping observations that will be used to study and constrain the initial velocity dispersion of the sodium source atoms at the exobase.

To investigate the nature of the initial velocity dispersion of the sodium source, two different source flux speed distributions discussed by Smyth and Combi (1988b; see their Appendix D) are considered: (1) a Maxwell-Boltzmann flux distribution and (2) a modified-

sputtering flux distribution. The Maxwell-Boltzmann flux distribution $\phi(v; T)$ is based on the Maxwell-Boltzmann velocity distribution and is defined as follows:

$$\phi(v; T) = \phi_0 \left(\frac{R_s}{R_E} \right)^2 \frac{2}{v_T} \left(\frac{v}{v_T} \right)^3 e^{-\left(\frac{v}{v_T} \right)^2}$$

where

$$v_T = \left(\frac{2kT}{m} \right)^{1/2}$$

is the most probable speed of the velocity distribution for an atom of mass m . The Maxwell-Boltzmann flux distribution is proportional to the local velocity integrated flux ϕ_0 referenced here to the satellite radius R_s not the exobase radius R_E and depends upon one parameter, the exobase temperature T (or alternatively v_T), which determines both the most probable speed v_m

$$v_m = \left(\frac{3kT}{m} \right)^{1/2}$$

and the speed dispersion of the flux distribution. The modified-sputtering flux distribution $\phi(v; \alpha, v_M, v_b)$ is proportional to the local velocity integrated flux ϕ_0 and depends upon three parameters: an exponent α , a velocity parameter v_b , and the velocity parameter v_M :

$$\phi(v; \alpha, v_M, v_b) = \phi_0 \left(\frac{R_s}{R_E} \right)^2 \frac{1}{v_b D(\alpha, v_M/v_b)} \left(\frac{v}{v_b} \right)^3 \left(\frac{v_b^2}{v^2 + v_b^2} \right)^\alpha \left[1 - \left(\frac{v^2 + v_b^2}{v_M^2} \right)^{1/2} \right],$$

where $D(\alpha, v_M/v_b)$ is a normalization constant (see Smyth and Combi 1988b). The exponent α primarily determines the dispersion of the distribution, which has a greater high-speed population as α decreases. The exponent α has a value of 3 for a classical sputtering distribution (i.e., representing a complete collisional cascade process) and a value of 7/3 for a Thomas-Fermi modified-sputtering flux distribution (i.e., representing the limit of a single elastic collisional ejection process), where the latter distribution is based upon a Thomas-Fermi differential scattering cross section. The velocity parameter v_b is related nonlinearly to the most probable speed v_m of the flux speed distribution and primarily determines v_m (see Smyth and Combi 1988b, Appendix D). The velocity parameter v_M primarily determines the maximum speed for the flux distribution and depends upon the maximum relative speed (and masses) of the plasma torus ion and sodium atom. The Maxwell-Boltzmann flux distribution and the modified-sputtering flux distribution, normalized to unit area, are each shown in Figure 8 for two different values of their parameters. The four flux distributions in Figure 8 will be utilized in the subsequent modeling analysis.

In calculating the column density and the D₂ emission brightness in the numerical sodium cloud model, a smaller two-dimensional sky-plane grid centered on Io ($\pm 15 R_{Io}$) is used to cover a spatial scale near the satellite more appropriate to the eclipse data while a much larger two-dimensional sky-plane grid centered on Io is used to cover a larger spatial scale more appropriate for the emission data and the sodium cloud image data. A one-dimensional profile for the eclipse data is obtained from the smaller two-dimensional sky-plane grid by extracting an average radial profile. This average radial profile will be called the calculated eclipse profile and will be denoted by the filled circles in Figures 9-14. A one-dimensional east-west D₂ brightness profile (and also a corresponding column density

profile) for the emission data and the sodium cloud image data is obtained from the larger two-dimensional sky-plane grid by selecting only the east-west grid elements that occur in the grid row containing Io. In Figures 9-14, the calculated east-west brightness and column density profiles are denoted by filled triangles for the forward cloud profile and by filled squares for the trailing cloud profile. To construct an eclipse or east-west profile, monoenergetic model calculations are performed for 18 different nonuniformly-spaced speeds ranging from 0.4 km sec^{-1} to 10 km sec^{-1} . Profiles for speeds beyond 10 km sec^{-1} are determined by an inverse speed extrapolation of the model results. The individual profiles for the different speeds are appropriately weighted for a given source flux speed distribution and then added to obtain the final spatial profile. Model calculations are performed for an Io geocentric phase angle of 92.9 degrees and an Io System III longitude angle of 48.6 degrees. These satellite conditions are similar to those for the emission 4 and eclipse 2 observations of Table 1, which are the observation closest to the eastern elongation point. This choice is also appropriate for all the eclipse data within the Lagrange sphere, which has no discernible dependence on these two Io related angles, and for the Io sodium cloud image data which have east-west profile areas in Figure 3 that are representative of the satellite near its orbital elongation points.

Model calculations for a Maxwell-Boltzmann flux distribution are presented in Figure 9 and Figure 10. In Figure 9a and Figure 9b, the calculated and measured sodium column density for the eclipse observations are compared for two different exobase temperatures. In Figure 10a and Figure 10b, the calculated D₂ emission brightness profiles for the forward and trailing clouds are compared to the emission 4 measurement profiles and to the sodium cloud image data profile areas for the same two exobase temperatures adopted, respectively, in Figures 9a and 9b.

For a Maxwell-Boltzmann flux distribution with a most probable speed of $v_m = 1.3 \text{ km sec}^{-1}$ (i.e., an exobase temperature of $\sim 1600 \text{ K}$, see Figure 8) and a total flux ϕ_0 (referenced to Io's surface area) of $3.0 \times 10^8 \text{ atoms cm}^{-2} \text{ sec}^{-1}$ (i.e., a total source of $\sim 1.2 \times 10^{26} \text{ atoms sec}^{-1}$), the model calculated column density and D_2 emission brightness profiles are shown in Figure 9a and Figure 10a, respectively. In Figure 9a for radial distances from the exobase to the Lagrange sphere, the model column density for the calculated eclipse profile (filled circles) provides an excellent fit to the eclipse observations (open circles) and also compares very favorably with the east-west column density profiles calculated for the forward (filled triangle) and trailing cloud (filled squares). In Figure 9a beyond the Lagrange sphere, however, all three of these calculated profiles fall below the eclipse observations. At and beyond about $8 R_{\text{Io}}$, the calculated east-west forward and trailing profiles rise above the calculated eclipse profile (because the column density is no longer spherically symmetric about Io), with the forward cloud profile having the largest column density and showing a distinct change in its slope compared to the trailing cloud profile. The corresponding model profiles for the D_2 emission brightness are given in Figure 10a. For both the forward and trailing profiles, the calculated eclipse and calculated east-west profiles are in good agreement with each other inside the Lagrange radius, with a maximum brightness of about 200 kR near the exobase. The calculated east-west profile threads the three emission 4 data points for the forward cloud, but falls well below the emission 4 data points in the trailing cloud. For both the forward and trailing clouds at larger radial distances, the calculated east-west profiles fall well below the areas for both the forward and trailing cloud images. This behavior indicates that there is a deficiency in the high-speed population of this source flux speed distribution at the exobase.

Model calculations were therefore performed for a Maxwell-Boltzmann flux distribution with a higher most probable speed of $v_m = 2.0 \text{ km sec}^{-1}$ (i.e., a exobase temperature of $\sim 3700 \text{ K}$, see Figure 8) and with a total flux ϕ_0 of $1.8 \times 10^8 \text{ atoms cm}^{-2} \text{ sec}^{-1}$ (i.e., a total source of $\sim 0.75 \times 10^{26} \text{ atoms sec}^{-1}$) and are shown in Figure 9b and Figure 10b. For the D_2 emission brightness profiles in Figure 10b, the calculated east-west profile now threads the center of the forward cloud image area for a radial distance up to about $70 R_{\text{Io}}$ and the lower trailing cloud image area for a radial distance of about $25 R_{\text{Io}}$ before it falls off too steeply. This improved fit at larger radial distances, however, reduces the D_2 emission brightness at the exobase to about 80 kR in Figure 10b and causes the calculated eclipse profile in Figure 9b to fall below the measured eclipse profile for radial distances inside of about $3 R_{\text{Io}}$. The Maxwell-Boltzmann flux distribution therefore cannot fit both the corona profile near Io and the sodium cloud east-west profiles at large distances from the satellite. A flux distribution that has a broader dispersion with enhanced populations for both the low-speed and high-speed atoms is required. The modified-sputtering flux distribution, which has a broader dispersion, is therefore considered in the remainder of the paper.

Model calculations for a classical sputtering flux distribution (i.e., $\alpha=3$) and a modified-sputtering flux distribution (i.e., $\alpha=7/3$, having even a larger high-speed population) are presented in Figure 11a and Figure 11b for the eclipse observations and in Figure 12a and Figure 12b for the emission 4 and sodium cloud east-west D_2 emission brightness profiles. For the two flux distributions, the most probable speed is, respectively, 1.0 km sec^{-1} and 0.5 km sec^{-1} , and the total flux ϕ_0 is, respectively, $3.2 \times 10^8 \text{ atoms cm}^{-2} \text{ sec}^{-1}$ (i.e., a total source of $\sim 1.3 \times 10^{26} \text{ atoms sec}^{-1}$) and $4.2 \times 10^8 \text{ atoms cm}^{-2} \text{ sec}^{-1}$ (i.e., a total source of $\sim 1.7 \times 10^{26} \text{ atoms sec}^{-1}$). In Figure 11, both sputtering flux distributions provide a reasonably good fit to the observed column density profile from

the exobase to radial distances of $\sim 8 R_{I0}$, just beyond the Lagrange radius. A careful comparison of Figure 11a and Figure 11b shows that the calculated sodium column density for the classical sputtering flux distribution is slightly larger within the Lagrange radius and is somewhat smaller beyond the Lagrange radius (as is to be expected), with the largest differences occurring in the trailing cloud profile beyond about $10 R_{I0}$.

For these two sputtering flux distributions, the same general behavior is seen in comparing the two calculated D₂ emission brightness profiles in Figure 12a and Figure 12b. For the classical sputtering flux distribution in Figure 12a, the calculated D₂ emission brightness profiles for the forward profile is slightly above the measured data point inside the Lagrange radius, matches the two measured data points beyond the Lagrange radius, and then threads the forward cloud image area nicely between about $20 R_{I0}$ and $80 R_{I0}$ before it falls too rapidly and drops below this area. An improved fit for the forward profile is provided by the modified sputtering distribution ($\alpha=7/3$) in Figure 12b. The calculated D₂ emission brightness profile for the forward profile in Figure 12b matches the measured data point inside the Lagrange radius, matches the two measured data points beyond the Lagrange radius, and then nicely threads the forward cloud image area all the way to $100 R_{I0}$. For the trailing profile and the classical sputtering flux distribution in Figure 12a, the calculated D₂ emission brightness profile matches the measured data point inside the Lagrange radius, is slightly below the two measured data point outside the Lagrange radius, and then threads the lower of the two trailing cloud image areas nicely between about $15 R_{I0}$ and $35 R_{I0}$ before it falls too rapidly and drops below this area. An improved fit is also provided for the trailing profile by the modified sputtering distribution in Figure 12b. The calculated D₂ emission brightness profile for the trailing profile in Figure 12b matches the measured data point inside the Lagrange radius, is slightly below

the two measured data point outside the Lagrange radius, and then threads the lower of the two trailing cloud image areas nicely all the way to $100 R_{I0}$. The lower of the two trailing cloud image areas corresponds to the east-west sodium cloud profile when the directional feature is oriented either north or south (i.e., above or below the east-west line or null location). For this non-null condition, it is particularly noteworthy that the spatially-isotropic ejection of sodium from the exobase with a modified sputtering flux distribution with $\alpha=7/3$ provides an excellent fit to the combined eclipse, emission, and forward/trailing sodium cloud image profile data from $1.4 R_{I0}$ to $100 R_{I0}$.

The measured trailing data points in Figure 12b were, however, acquired at the null condition and are consistent with the upper of the two trailing cloud image areas also acquired at the null condition. In order to fit the trailing profile for the null condition, it is then clear that a flux distribution is required with an even more enhanced high-speed population than the modified sputtering flux distribution with $\alpha=7/3$. Since the modified sputtering flux distribution for $\alpha=7/3$ corresponds to the limit of a single collision cascade process described by a Thomas-Fermi cross section (see Smyth and Combi 1988b), reducing the value of α to a smaller value becomes somewhat physically questionable but may be done for practical purposes of illustrating the impact of an enhanced high-speed population in the model calculation.

For a modified sputtering flux distribution with $\alpha=2$, a most probable speed of 0.4 km sec^{-1} , and an isotropic exobase source rate of $1.9 \times 10^{26} \text{ atoms sec}^{-1}$ (i.e., a total flux ϕ_0 of $4.7 \times 10^8 \text{ atoms cm}^{-2} \text{ sec}^{-1}$), the model-data comparison is shown in Figure 13 for the eclipse column density and in Figure 14 for the emission and sodium cloud east-west D_2 emission brightness profiles. In Figure 13, the sputtering flux distribution provides a reasonably good fit to the observed column density data points with only a small departure

very near the exobase and produces a column density profile beyond $10 R_{Io}$ that is significantly enhanced compared to the $\alpha=7/3$ case in Figure 11b. In Figure 14, the calculated D₂ emission brightness profile for the forward profile is significantly above the measured data point both inside and outside the Lagrange radius and is above or in the very top of the forward cloud image area all the way to $100 R_{Io}$. The additional enhanced high-speed population of the $\alpha=2$ modified sputtering flux distribution is too large and therefore not consistent with the observed forward profile. In contrast for the trailing profile in Figure 14, the calculated D₂ emission brightness profile matches the measured data point inside and outside of the Lagrange radius very well and then threads the upper of the two trailing cloud image areas nicely all the way to $\sim 90 R_{Io}$. This demonstrates that the trailing cloud can be fitted with an enhanced high-speed population of sodium atoms in the flux distribution. It also immediately demonstrates that the flux distribution at the exobase must be nonisotropic with some of the enhanced high-speed population weighted more toward vector directions that will preferentially populate the trailing cloud rather than the forward cloud. This nonisotropic requirement for a flux distribution for speeds of $\sim 20 \text{ km sec}^{-1}$ is consistent with the conclusion reached by the modeling analysis of observations for the north-south oscillating directional features by Pilcher *et al.* (1984). In this analysis, their $\sim 20 \text{ km sec}^{-1}$ sodium was constrained to be initially directed at near right angles to Io's orbital motion and hence was angularly deficient in the forward direction of motion of the satellite and (more importantly) in the trailing apex direction, which preferentially populates the forward cloud.

4. DISCUSSION AND CONCLUSIONS

The composite spatial information for sodium obtained by combining the eclipse observations (radial distances from Io of $1.4 R_{Io}$ to $\sim 10 R_{Io}$), the emission observations (east-west distances of $\pm 4 R_{Io}$ to $\pm 40 R_{Io}$) and the sodium cloud observations (east-west distances of $\pm 10 R_{Io}$ to $\pm 100 R_{Io}$) has been analyzed to extract a basic description for the flux speed distribution at the satellite's exobase. An isotropic modified-sputtering flux speed distribution with $\alpha=7/3$, a most probable speed of 0.5 km sec^{-1} , and a source strength of $1.7 \times 10^{26} \text{ atoms sec}^{-1}$ provided a very good fit to these composite observations when the directional feature is either north or south and hence not contributing to east-west profile of the trailing cloud. It is remarkable that these observations, acquired by a number of ground-based programs over very different spatial scales and at different times during the 1975-1985 decade, are so self consistent. Near Io, the two-dimensional sodium column density produced by this modified sputtering distribution as calculated by the sodium cloud model in the profile analysis above is shown in Figure 15 and can be seen at larger distances from Io to become nonspherical and more confined near the satellite plane. This flattening near the satellite plane is the merging of the near Io corona into the sodium cloud and is caused naturally by orbital dynamics beyond the satellite Lagrange sphere where the gravity of Jupiter is dominant. This merging and its spatial extension into the forward sodium cloud is reproduced very well by the isotropic modified sputtering distribution. The forward cloud portion of the east-west emission data profiles has a rather tightly confined slope that, in the absence of the trailing cloud enhancement at the null condition, is less steep and is brighter than the trailing cloud profiles. In order, however, to reproduce the extended east-west profile in the trailing sodium cloud when the directional feature is in the satellite plane (i.e., the null condition), additional nonisotropic high-speed

sodium is required and is generally consistent with the earlier modeling of the directional feature (Pilcher *et al.* 1984).

The sodium atoms ejected from Io's exobase as described above by the modified sputtering flux distribution have speeds primarily in the range from 0 to a few 10's km sec⁻¹. This neutral flux distribution represents the spatially integrated effect of the incomplete collisional cascade process that occurs from the collisional interactions of heavy-ions in the corotating plasma torus with neutrals in Io's atmosphere. This flux speed distribution can be alternatively described as a source rate speed distribution by multiplying it by the satellite surface area. In addition to these ion-neutral elastic collisional encounters, resonance charge exchange between plasma torus sodium ions and neutral sodium in Io's atmosphere (i.e., $\text{Na} + \text{Na}^+ \rightarrow \text{Na}^+ + \text{Na}$) is also responsible for producing sodium atoms with higher speeds relative to Io. These speeds are centered about the corotational ion speed (~ 60 km sec⁻¹) relative to Io's motion and have a dispersion reaching from several 10's km sec⁻¹ to ~ 100 km sec⁻¹. This higher-speed source of sodium atoms together with some lower speed (~ 15 - 20 km sec⁻¹) sodium atoms associated with the nonisotropic source for the directional feature have been shown in modeling studies (Smyth and Combi 1991; Flynn *et al.* 1992) to accurately reproduce the image of sodium in the (D₁+D₂) emission line brightness measured on a radial scale of ± 400 - 500 planetary radii about Jupiter by Mendillo *et al.* (1990). This large scale distribution of sodium has been called the magneto-nebula or sodium zenocorona. Modeling studies for this image indicated that the higher-speed source was $\sim 2 \times 10^{26}$ atoms sec⁻¹ while the lower speed source was $\sim 1 \times 10^{26}$ atoms sec⁻¹. More recent observations and analysis for the sodium zenocorona images (Flynn *et al.* 1993) have shown that the source strength for the higher-speed sodium source is time variable with values usually in the range ~ 2 - 4×10^{26} atoms sec⁻¹. In addition, a recent analysis by Wilson (1993, private communication) of images

for the narrow forward jet of sodium observed by Schneider *et al.* (1991) has shown that this spatially distributed source is time variable and typically contributes a few times 10^{25} atoms sec^{-1} to the higher speed sodium source for the zenocorona. A typical total source rate speed distribution for sodium at Io's exobase can therefore be constructed by combining the modified sputtering source rate distribution determined in this paper with the charge exchange source rate distribution for the zenocorona (see Smyth and Combi 1991). This total source rate speed distribution function is shown in Figure 16, where the lower (solid line) and upper (dashed line) curves correspond, respectively, to the sodium zenocorona higher-speed source rate of 2.2×10^{26} atoms sec^{-1} as determined by Smyth and Combi (1991) from January 1990 image data and 4×10^{26} atoms sec^{-1} as determined by Flynn *et al.* (1993) from February 1991 image data.

The total source rate speed distribution functions at Io's exobase expected for other atomic species, such as K, O, and S, can be constructed in a similar fashion to sodium by adopting the estimated source rates for the modified sputtering distribution and the charge exchange distribution given by Smyth and Combi (1991). The main differences in the total source rate speed distribution functions will arise from the relative importance of the source strengths for the modified sputtering and charge exchange processes. The relative importance of the higher speed source to the lower speed source would be much smaller than sodium for K, because of the smaller number of K^+ ions in the plasma torus, and would be significantly larger than sodium for O and S, because of the much larger number of O and S ions in the plasma torus.

Future studies for the sodium flux speed distribution at Io's exobase are anticipated using a much larger emission data set for sodium (~ 100 profiles) acquired in 1987 and recently reduced by Schneider (1993, private communication) to a form suitable for

analysis. Because of the much larger data base, it will be possible in these studies to analyze the combined spatial and spectral information in order to refine the nonisotropic nature of the flux distribution and also to search for possible east-west and System III modulations in the flux speed distribution. Once this information is determined for sodium, the implications for the more abundant species in Io's atmosphere will be particularly important in other related studies for the many faceted and complex phenomena in the Io-Jupiter system.

ACKNOWLEDGMENTS

We are grateful to N. M. Schneider for helpful discussions and for providing the numerical data for the 1985 emission observations. This research was supported by the Planetary Atmospheres Program of the National Aeronautical and Space Administration under grant NAGW-3585 to the University of Michigan and under contracts NASW-4416 and NASW-4471 to Atmospheric and Environmental Research, Inc.

REFERENCES

- Bergstralh, J. T., D. L. Matson, and T. V. Johnson 1975. Sodium D-Line Emission from Io: Synoptic Observations from Table Mountain Observatory. *Astrophys. J. Lett.* **195**, L-131-L135.
- Bergstralh, J. T., J. W. Young, D. L. Matson, and T. V. Johnson 1977. Sodium D-Line Emission from Io: A Second Year of Synoptic Observation from Table Mountain Observatory. *Astrophys. J. Lett.* **211**, L51-L55.
- Brown, R. A., and Y. L. Yung 1976. Io, Its Atmosphere and Optical Emissions. In *Jupiter Studies of the Interior, Atmosphere, Magnetosphere, and Satellites* (T. Gehrels, Ed.), pp. 1102-1145. Univ. of Arizona Press, Tucson.
- Flynn, B., M. Mendillo, and J. Bumgardner 1992. Observations and Modeling of the Jovian Remote Sodium Emission. *Icarus* **99**, 115-130.
- Flynn, B., M. Mendillo, and J. Bumgardner 1993. The Jovian Sodium Nebula: Two Years of Ground-Based Observations. preprint.
- Goldberg, B. A., Yu. Mekler, R. W. Carlson, T. V. Johnson, and D. L. Matson 1980. Io's Sodium Emission Cloud and the Voyager 1 Encounter. *Icarus* **44**, 305-317.
- Goldberg, B. A., G. W. Garneau, and S. K. LaVoie 1984. Io's Sodium Cloud. *Science* **226**, 512-516.

Goldberg, B. A. and Smyth, W. H. 1993. The JPL Table Mountain Io Sodium Cloud Data Set. Paper in preparation.

Matson, D. L., B. A. Goldberg, T. V. Johnson, and R. W. Carlson 1978. Images of Io's Sodium Cloud. *Science* **199**, 531-533.

Mendillo, M., J. Baumgardner, B. Flynn and W. J. Hughes 1990. The Extended Sodium Nebula of Jupiter. *Nature*, **348**, 312-314.

Murcray, F. J. 1978. Observations of Io's Sodium Cloud, Ph. D. Thesis, Dept. of Physics, Harvard University.

Murcray, F. J. and R. M. Goody 1978. Pictures of the Io Sodium Cloud. *Ap. J.*, **226**, 327- 335.

Pilcher, C. B., W. H. Smyth, M. R. Combi, and J. H. Fertel 1984. Io's Sodium Directional Features: Evidence for a Magnetospheric-Wind-Driven Gas Escape Mechanism. *Ap. J.*, **287**, 427-444.

Schneider, N. M. 1988. Sodium in Io's Extended Atmosphere. Ph.D. Thesis, Department of Planetary Sciences, Univ. of Arizona.

Schneider, N. M., D. M. Hunten, W. K. Wells, and L. M. Trafton 1987. Eclipse Measurements of Io's Sodium Atmosphere. *Science*, **238**, 55-58.

Schneider, N. M., D. M. Hunten, W. K. Wells, A. B. Schultz, and U. Fink 1991. The Structure of Io's Corona. *Ap. J.*, **368**, 298-315.

Smyth, W. H. and M. R. Combi 1987. Nature of Io's Atmosphere and its Interaction with the Planetary Magnetosphere. *BAAS*, **19**, 855.

Smyth, W. H. and M. R. Combi 1988a. A General Model for Io's Neutral Gas Cloud. I. Mathematical Description. *Ap. J. Supp.*, **66**, 397-411.

Smyth, W. H. and M. R. Combi 1988b. A General Model for Io's Neutral Gas Clouds. II. Application to the Sodium Cloud. *Ap. J.*, **328**, 888-918.

Smyth, W. H. and M. R. Combi 1991. The Sodium Zenocorona. *JGR*, **96**, 22711-22727.

Smyth, W. H. and B. A. Goldberg 1993. The Io Sodium Cloud: Space-Time Signatures of East-West and System III Longitudinal Asymmetries in the Jovian Magnetosphere. Paper presented at the Io: An International Conference, San Juan Capistrano, California, June 22-25.

Smyth, W. H., and M. B. McElroy 1978. Io's Sodium Cloud: Comparison of Models and Two-Dimensional Images. *Astrophys. J.* **226**, 336-346.

Table 1

1985 Io Eclipse and Emission Measurements

Date	UT Midpoint	Io Geocentric Phase Angle Range (deg)	Io System III Longitude Range (deg)	Spectrum ID	Eclipse	Type of Observation Emission
August 27	0714	61.4 ± 0.7	29.9 ± 2.3	85g188	1	1
	0720	62.3 ± 11.0	32.9 ± 35.8	a		
	0830	72.2 ± 1.1	65.1 ± 3.4	85g196		2
September 13	0641	276.6 ± 0.7	194.7 ± 2.3	85h032		3
September 14	0245	87.7 ± 0.7	31.4 ± 2.3	85h102	2	4
	0326	93.5 ± 4.2	50.5 ± 13.7	b		
	0416	100.6 ± 0.4	73.6 ± 1.4	85h113		5
September 15	0316	294.7 ± 0.7	353.7 ± 3.0	85h152	3	6
	0500	309.4 ± 11.5	41.7 ± 37.4	c		
September 21	0604	100.5 ± 1.6	112.5 ± 5.2	d	4	
September 23	0230	117.2 ± 0.7	267.6 ± 2.3	85h433	5	7
	0301	121.6 ± 0.4	281.9 ± 1.2	85h436		8
	0356	129.3 ± 2.0	307.3 ± 6.7	e		
	0534	143.1 ± 0.7	352.9 ± 2.3	85h457		9

a. Eclipse 1 : 85g179, 85g181, 85g185, 85g188, 85g192, 85g193, 85g196

b. Eclipse 2 : 85h103, 85h104, 85h105, 85h106, 85h107, 85h108, 85h109, 85h110, 85h112

c. Eclipse 3 : 85h153, 85h154, 85h155, 85h157, 85h159, 85h162, 85h163

d. Eclipse 4 : 85h287, 85h288, 85h289, 85h290, 85h291, 85h292, 85h293, 85h294, 85h295

e. Eclipse 5 : 85h441, 85h442, 85h443, 85h444, 85h445, 85h446, 85h447, 85h448, 85h449, 85h450

Table 2. 1985 Emission Data

Radial Distance From Io (satellite radii)	D ₂ Intensity (kR)								
	Emission 1 61.4° 27 August (85g188)	Emission 2 72.2° 27 August (85g196)	Emission 4 87.7° 14 September (85h102)	Emission 5 100.6° 14 September (85h113)	Emission 7 117.2° 23 September (85h433)	Emission 8 121.6° 23 September (85h436)	Emission 9 143.1° 23 September (85h457)	Emission 3* 276.6° 13 September (85h032)	Emission 6 294.7° 15 September (85h152)
-29.92					0.69	0.93	0.66		1.12
-29.65								1.40	
-24.48					1.19	0.84	0.95	2.22	
-21.76					1.38	2.10	1.74		2.15
-16.32				1.91					
-15.78					2.90	3.29	3.38	4.40	
-14.96					7.49	7.76	7.54	1.54	
-10.88	3.16		3.17					28.69	18.75
-9.52	5.21	4.50	6.41					45.47	
-6.80	14.65	11.29	14.71					48.61	
-3.81	24.31	18.39	24.12		25.61	25.01	21.00		
-2.18	27.46	19.99	27.14		29.95	28.72	23.89		24.85
-1.09					27.90	30.16	23.97	45.56	
-0.82	27.44	19.19	27.14						25.27
0.00					26.31	26.39	22.84	39.45	
0.27	25.87	19.35	26.65	23.03	22.42	23.91	20.21	33.60	22.90
1.09									
1.36	25.19	16.87	25.68	19.60	15.54	14.83	12.52	20.06	11.53
2.18					7.09	7.10	6.02	7.52	4.79
3.26	17.60	11.92	18.10	11.87					
4.08					5.52	5.52	5.52	7.52	1.66
5.98	8.31	5.52	8.17	5.52	2.47	2.47	2.26	2.73	0.77
6.80									
10.06	3.40	1.94	3.84	3.21	1.03	1.11	0.82	1.39	
10.88			2.84	1.81	0.68	0.75	0.52		
15.50			2.25						
16.32									
21.76									
23.66				1.24				1.06	0.53
24.48									
27.20			1.39					1.00	
35.36			1.27					0.83	
46.24									

*calibration uncertain

Table 3

Power Law Fit to the D₂ Emission Profiles for Io East of Jupiter[†]

Date	Io Geocentric Phase Angle (deg)	Io System III Longitude (deg)	Exponent		Amplitude (kR)	
			East Profile	West Profile	East Profile	West Profile
August 27	61.4	29.9	1.67 (F)	1.57 (T)	191	124
	72.2	65.1	1.85 (S)	1.80 (S)	169	142
September 14	87.7	31.4	1.23 (S/T)	1.80 (S/F)	89	188
	100.6	73.6	1.27 (T)	--	66	--
September 23	117.2	267.6	2.05 (T)	1.57 (F)	342	135
	121.6	281.9	1.96 (T)	1.54 (F)	283	138
	143.1	352.9	2.16 (T)	1.64 (F)	374	165

[†] Profile points inside of 4 R_{Io} are excluded

F = forward cloud; S = symmetric turning point; T = trailing cloud.

Table 4
East-West D2 Brightness Profiles for Sodium Cloud Image Data

LT Date	LT Time	Image ID Number	Io Geocentric Phase Angle (deg)	Io System III Longitude (deg)	East-West Distance from Io for Specified D ₂ Brightness Level (satellite radii)											
Image Data Set Reference: Murcray (1976)					0.5 kR			1.0 kR			1.5 kR			2.0 kR		
1976 Nov. 16	0806	ES 3288	256	262	Forward	Trailing		Forward	Trailing		Forward	Trailing		Forward	Trailing	
1977 Jan 27	0024	ES 369A	86	193	60	38		51	29		46	24		28	14	
	0217	ES 370D	102	245	>83	30		56	22		44	19		32	16	
									25		46	21		24	19	
Image Data Set Reference: Goldberg and Smyth (1993)					0.2 kR			0.5 kR			1.0 kR			2.0 kR		
1981 May 5	0819	SIP 418/31-33	102	300	Forward	Trailing		Forward	Trailing		Forward	Trailing		Forward	Trailing	
May 12	0848	SIP 420/30-32	91	302	78	69		63	40-66		45	37		24	21	
May 13	0346	SIP 421/21-23	253	108	66	86		41	37		35	29		20	21	
	0555	SIP 421/32-33	271	168	74-103	73		70	41		41	27		29	20	
June 6	0436	SIP 424/10-12	103	300	124	65		112	44		51	30		26	19	
					81	75		68	71		36	26		20	23	
Image Data Set Reference: Morgen (1984)					0.3 kR			0.6 kR			0.9 kR			1.8 kR		
1983 June 13	0714	18492	274	230	Forward	Trailing		Forward	Trailing		Forward	Trailing		Forward	Trailing	
	0722	18494	275	233	--	39		58	26		37	19		20	--	
	0729	18496	276	237	--	35		52	22		40	20		20	--	
	0827	18501	284	264	>93	36		52	22		37	17		22	--	
	0949	18509	296	301	>93	39		61	25		42	19		23	--	
	1010	18511	299	311	>93	47		63	26		44	17		24	--	
					>93	41		63	23		44	16		19	--	

Table 5

1985 Io Emission Measurements

Emission	Date	Io Geocentric Phase Angle Range (deg)	Io System III Longitude Range (deg)	Directional Feature Orientation	Dominant Spatial Profile	Enhanced Doppler Signatures
1	August 27	61.4 \pm 0.7	29.9 \pm 2.3	null south	similar symmetric	trailing/forward no
2		72.2 \pm 1.1	65.1 \pm 3.4			
3	September 13	276.6 \pm 0.7	194.7 \pm 2.3	null/north	similar	trailing
4	September 14	87.7 \pm 0.7	31.4 \pm 2.3	null south	trailing ---	trailing no
5		100.6 \pm 0.4	73.6 \pm 1.4			
6	September 15	294.7 \pm 0.7	353.7 \pm 3.0	null	trailing	trailing
7	September 23	117.2 \pm 0.7	267.6 \pm 2.3	north	forward	no
8		121.6 \pm 0.4	281.9 \pm 1.2	north	forward	no
9		143.1 \pm 0.7	352.9 \pm 2.3	null	forward	no

FIGURE CAPTIONS

FIG. 1. 1985 Eclipse Data. The sodium column density is shown as a function of the radial distance from the center of Io for the five eclipse measurements acquired by Schneider *et al.* (1991). The position of the nominal exobase and the average Lagrange radius are indicated.

FIG. 2. 1985 Emission Data. The sodium D₂ emission brightness in units of kiloRayleighs is shown as a function of the east-west distance from the center of Io along the observing slit for the nine emission observations summarized in Table 3 and acquired by Schneider *et al.* (1991).

FIG. 3. Selected East and West Brightness Profiles for the 1985 Emission Data. The spatial profiles both east and west of Io for the sodium D₂ emission brightness in units of kiloRayleighs are shown as a function of the distance along the observing slit from the center of Io for five emission observations identified by their satellite geocentric phase angle. These five profiles occur when Io is east of Jupiter and just past the satellite phase angle where the forward cloud has its symmetric turning point so that the trailing cloud profiles are all to the east of Io and the forward cloud profiles are all to the west of Io. A power law fit to each profile is also shown. At larger distances from Io, an envelope for the east-west D₂ emission profile acquired from sodium image data is shown by the shaded area. For the trailing profile, the shaded area is divided into two parts, where the lower area corresponds to sodium cloud data where the directional feature is oriented either north or south and where the upper area corresponds to the directional feature oriented along the east-west direction (i.e., the null condition).

FIG. 4. System III Correlation for the North-South Orientation of the Sodium Cloud Directional Feature. The north and south orientation of the directional feature as determined by Goldberg and Smyth (1993) from a set of sodium D-line emission image observations is shown as a function of the System III longitude angle of Io. Note that image observations for Io east and west of Jupiter are identified, respectively, by open and filled squares.

FIG. 5. Io Sodium Cloud Images. Three calibrated D₂ emission images of the Io sodium cloud from the JPL Table Mountain Data Set are shown to proper scale with Jupiter and Io's orbit as viewed from earth in 1981 (Smyth and Goldberg 1993). The Io System III longitude and corresponding orientation of the trailing directional feature in image A are 247 degrees and north, in image B are 104 degrees and south, and in image C are 178 degrees and only very slightly north. An east-west spatial scale of ± 100 planetary radii about Io is shown for reference. Contour levels for the D₂ brightness, from outside to inside, are 0.2, 0.5, 1, 2, 4, 6, 8, and 10 kR.

FIG. 6. Monoenergetic Sodium Cloud Modeling of the 1985 Eclipse Data. The eclipse data points of Schneider *et al.* (1991) are shown by the open circles. The dots are calculated by the Io sodium cloud model of Smyth and Combi (1988b) for their case C description of the plasma torus with an east-west electric field of 2.8 mV m^{-1} in the Io frame and for an isotropic and radial ejection of 2.6 km sec^{-1} sodium atoms from an assumed exobase of 2600 km radius for a source strength of $6.2 \times 10^{25} \text{ atoms sec}^{-1}$. The calculation was performed for an Io geocentric phase angle of 92.9 degrees and an Io System III longitude angle of 48.6 degrees. The sodium source used here is typical of that required for this monoenergetic calculation to fit the D₂ emission brightness of the sodium cloud images at larger distances from Io.

FIG. 7. Effect of Lifetime on the Sodium Column Abundance. Two model calculations for the column abundance are compared with the eclipse data points (shown by the open circles) of Schneider *et al.* (1991). The plasma torus description adopted in the Io sodium cloud model is described in Fig. caption 6. The eclipse data points are fit outside and somewhat inside the Lagrange radius by the model for the minimum lifetime case (filled circles), which occurs for an Io phase angle of 90 degrees (eastern elongation), an Io System III magnetic longitude angle of 179 degrees, and a sodium source rate of 0.96×10^{26} atoms sec^{-1} . The same source rate is assumed for the maximum lifetime case (filled squares), which occurs for an Io phase of 270 degrees (western elongation) and an Io System III magnetic longitude angle of 299 degrees.

FIG. 8. Flux Speed Distribution Functions for Sodium at Io's Exobase. Maxwell-Boltzmann flux speed distribution for sodium are shown for a most probable speed, v_m , of 1.3 km sec^{-1} (short dashed line) and 2.0 km sec^{-1} (longer dashed line). Modified sputtering flux speed distributions are also shown for $\alpha = 3$ and a most probable speed of 1.0 km sec^{-1} (dotted line) and for $\alpha = 7/3$ and a most probable speed of 0.5 km sec^{-1} (solid line). All of the flux speed distributions are normalized to unit area.

FIG. 9. Model Calculations for the Io Eclipse Data Using a Maxwell-Boltzmann Flux Speed Distribution. The atomic sodium column density profile near Io determined from the 1985 eclipse data by Schneider *et al.* (1991) is shown by the open circles. The model calculated column density profiles are shown by solid dots for the (cylindrically-averaged) corona, by solid triangles for the forward cloud along the east-west slit direction, and by solid squares for the trailing cloud along the east-west slit direction. These column density profiles were calculated using the Io sodium cloud model of Smyth and Combi (1988b) for their case C

description of the plasma torus (see Fig. caption 6) and for an Io geocentric phase angle of 92.9 degrees and an Io System III longitude angle of 48.6 degrees, which are similar to the emission 4 observation conditions in Table 1. Sodium was ejected uniformly from an assumed exobase of 2600 km radius with a velocity dispersion for a Maxwell–Boltzmann flux distribution, where in (a) $v_m = 1.3 \text{ km sec}^{-1}$ and $\phi_0 = 3.0 \times 10^8 \text{ atom cm}^{-2} \text{ sec}^{-1}$, and in (b) $v_m = 2.0 \text{ km sec}^{-1}$, and $\phi_0 = 1.8 \times 10^8 \text{ atom cm}^{-2} \text{ sec}^{-1}$.

FIG. 10. Model Calculations for the East-West D2 Brightness Profiles Using a Maxwell-Boltzmann Flux Speed Distribution. The east-west D2 brightness profile near Io in both the trailing and forward cloud directions as determined by the emission 4 data of Schneider *et al.* (1991) are shown by the open circles. The east-west profile envelopes in both the trailing and forward cloud directions as determined from the sodium cloud image data are shown by the shaded areas (see Fig. caption 3). The descriptions of the symbols for the calculated profiles, the sodium cloud model and plasma torus, and the Maxwell–Boltzmann flux distribution in (a) and (b) are the same as in Fig. caption 9.

FIG. 11. Model Calculations for the Eclipse Data Using a Modified Sputtering Flux Speed Distribution. The atomic sodium column density profile near Io determined from the 1985 eclipse data by Schneider *et al.* (1991) is shown by the open circles. The model calculated column density profiles are shown by solid dots for the (cylindrically-averaged) corona, by solid triangles for the forward cloud along the east-west direction, and by solid squares for the trailing cloud along the east-west direction. These column density profiles were calculated using the Io sodium cloud model of Smyth and Combi (1988b) for their case C description of the plasma torus (see Fig. caption 6) and for an Io geocentric phase angle of 92.9 degrees and an Io System III longitude angle of 48.6 degrees, which are similar to the emission 4 observation conditions in Table 1. Sodium was ejected uniformly from an assumed exobase

of 2600 km radius with a velocity dispersion for a modified sputtering flux distribution, where in (a) $\alpha = 3$, $v_m = 1.0 \text{ km sec}^{-1}$, and $\phi_0 = 3.2 \times 10^8 \text{ atom cm}^{-2} \text{ sec}^{-1}$, and in (b) $\alpha = 7/3$, $v_m = 0.5 \text{ km sec}^{-1}$, and $\phi_0 = 4.2 \times 10^8 \text{ atom cm}^{-2} \text{ sec}^{-1}$.

FIG. 12. Model Calculations for the East-West D2 Brightness Profiles Using a Modified Sputtering Flux Speed Distribution. The east-west D2 brightness profile near Io in both the trailing and forward cloud directions determined by the emission 4 data of Schneider *et al.* (1991) are shown by the open circles. The east-west profile envelopes determined from the sodium cloud image data are shown by the shaded areas (see Fig. caption 3). The descriptions of the symbols for the calculated profiles, the sodium cloud model and plasma torus, and the modified sputtering flux distribution used in (a) and (b) are the same as in Fig. caption 11.

FIG. 13. Model Calculations for the Eclipse Data Using a Modified Sputtering Flux Speed Distribution. The atomic sodium column density profile near Io determined from the 1985 eclipse data by Schneider *et al.* (1991) is shown by the open circles. The model calculated column density profiles are shown by solid dots for the (cylindrically-averaged) corona, by solid triangles for the forward cloud along the east-west direction, and by solid squares for the trailing cloud along the east-west direction. These column density profiles were calculated using the Io sodium cloud model of Smyth and Combi (1988b) for their case C description of the plasma torus (see Fig. caption 6) and for an Io geocentric phase angle of 92.9 degrees and an Io System III longitude angle of 48.6 degrees, which are similar to the emission 4 observation conditions in Table 1. Sodium was ejected uniformly from an assumed exobase of 2600 km radius with a velocity dispersion for a modified sputtering flux distribution, where $\alpha = 2$, $v_m = 0.4 \text{ km sec}^{-1}$, and $\phi_0 = 4.7 \times 10^8 \text{ atom cm}^{-2} \text{ sec}^{-1}$.

FIG. 14. Model Calculations for the East-West D2 Brightness Profiles Using a Modified Sputtering Flux Speed Distribution. The east-west D2 brightness profile near Io in both the trailing and forward cloud directions determined by the emission 4 data of Schneider *et al.* (1991) are shown by the open circles. The east-west profile envelopes determined from the sodium cloud image data are shown by the shaded areas (see Fig. caption 3). The descriptions of the symbols for the calculated profiles, the sodium cloud model and plasma torus, and the modified sputtering flux distribution are the same as in Fig. caption 13.

FIG. 15. Two-Dimensional Nature of the Sodium Column Density in Io's Corona. Contours for the two-dimensional column density in Io's corona are shown in the sky-plane of the earth as determined from the sodium cloud model calculation for the modified sputtering flux speed distribution described in Fig. 11(b). The vertical and horizontal directions are the projected directions that are, respectively, perpendicular and parallel to the semi-major axis of the Io's orbital ellipse on the sky plane. The scale is in kilometers, and the small tick marks are separated by 1000 km. Io's location and size are shown to scale by the black circle. The sodium column density contours in units of 10^{11} atoms cm^{-2} are, from inside to outside, 7, 5, 3, 2, 1, 0.7, 0.5, 0.3, and 0.2.

FIG. 16. Total Source Rate Speed Distribution Function for Sodium at Io's Exobase. The total source rate speed distribution function at Io's exobase, in units of 10^{26} atoms sec^{-1} $(\text{km/sec})^{-1}$, is composed of three separate source rate speed distributions as discussed in the text and is shown for a smaller (solid line) and larger (dashed line) source strength for the higher-speed zenocorona source centered about 57 km sec^{-1} . The decomposition of the solid curve into its three separate source rate speed distributions is shown in the cutout and is determined by combining (1) the isotropic modified sputtering source rate distribution

(dotted line in the cutout) for $\alpha = 7/3$, $v_m = 0.5 \text{ km sec}^{-1}$ and a source strength of $1.75 \times 10^{26} \text{ atom sec}^{-1}$, (2) the nonisotropic lower-speed source rate distribution (short dashed line in the cutout) for the sodium zenocorona centered about 20 km sec^{-1} , with a source strength of $1.1 \times 10^{26} \text{ atoms sec}^{-1}$ as determined by Smyth and Combi (1991), and (3) the nonisotropic higher-speed source rate distribution (longer dashed line in the cutout) for the sodium zenocorona centered about 57 km sec^{-1} , with a source strength of $2.2 \times 10^{26} \text{ atoms sec}^{-1}$ as determined by Smyth and Combi (1991). The source rate speed distribution (dashed line) with the larger source strength for the higher-speed zenocorona source is determined in the same fashion with the exception that the higher-speed zenocorona source is increased to $4.0 \times 10^{26} \text{ atoms sec}^{-1}$, so as to exhibit the typical time-variable source range of $2\text{-}4 \times 10^{26} \text{ atoms sec}^{-1}$ reported by Flynn *et al.* (1993).

1985 Eclipse Data

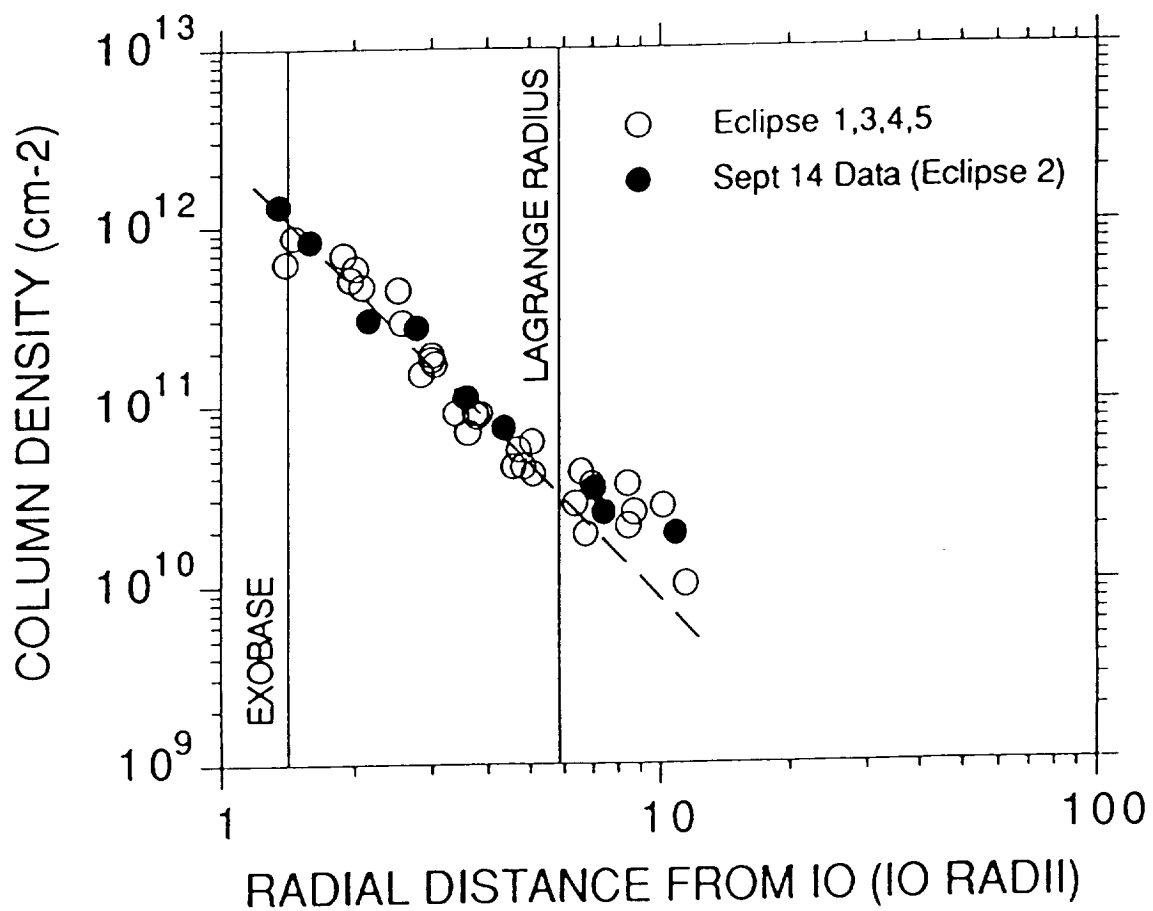


Figure 1

1985 Emission Data

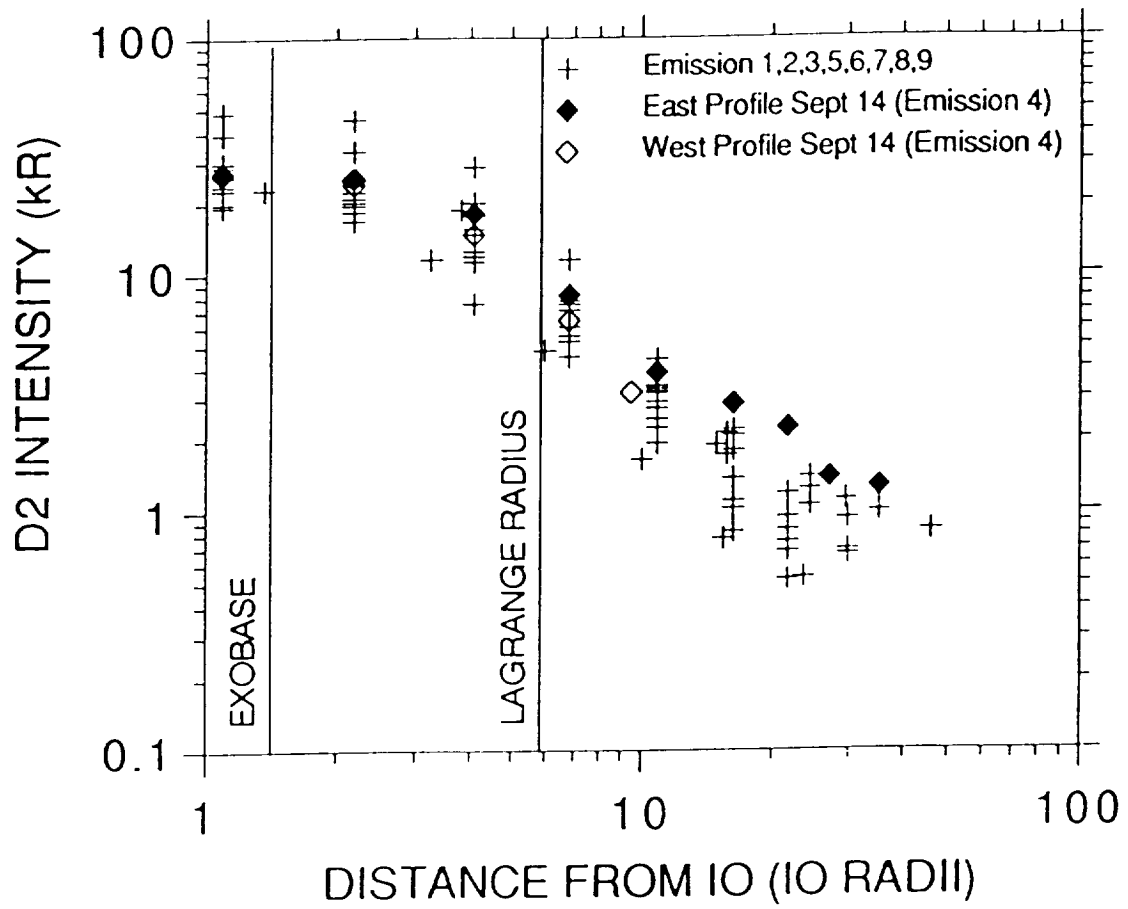


Figure 2

1985 EMISSION DATA

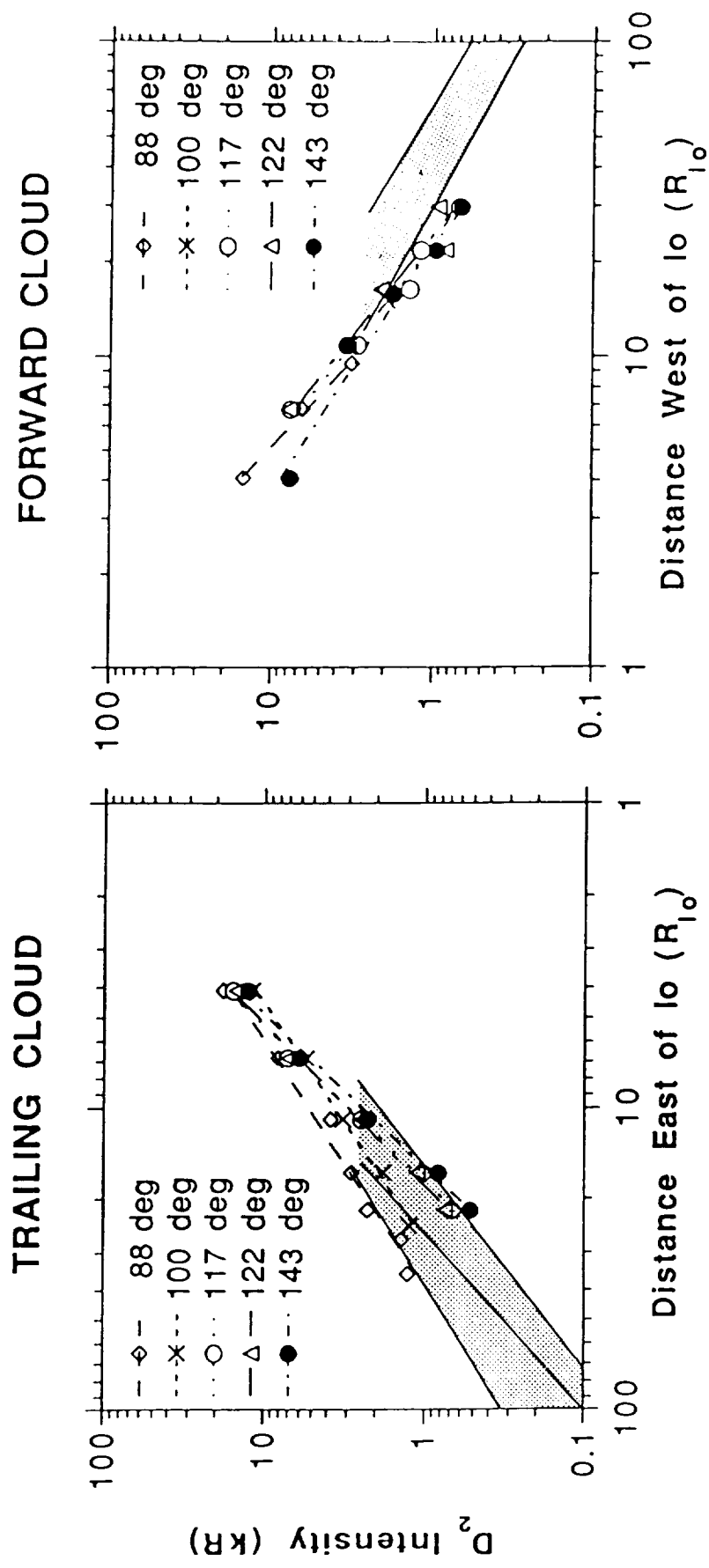


Figure 3

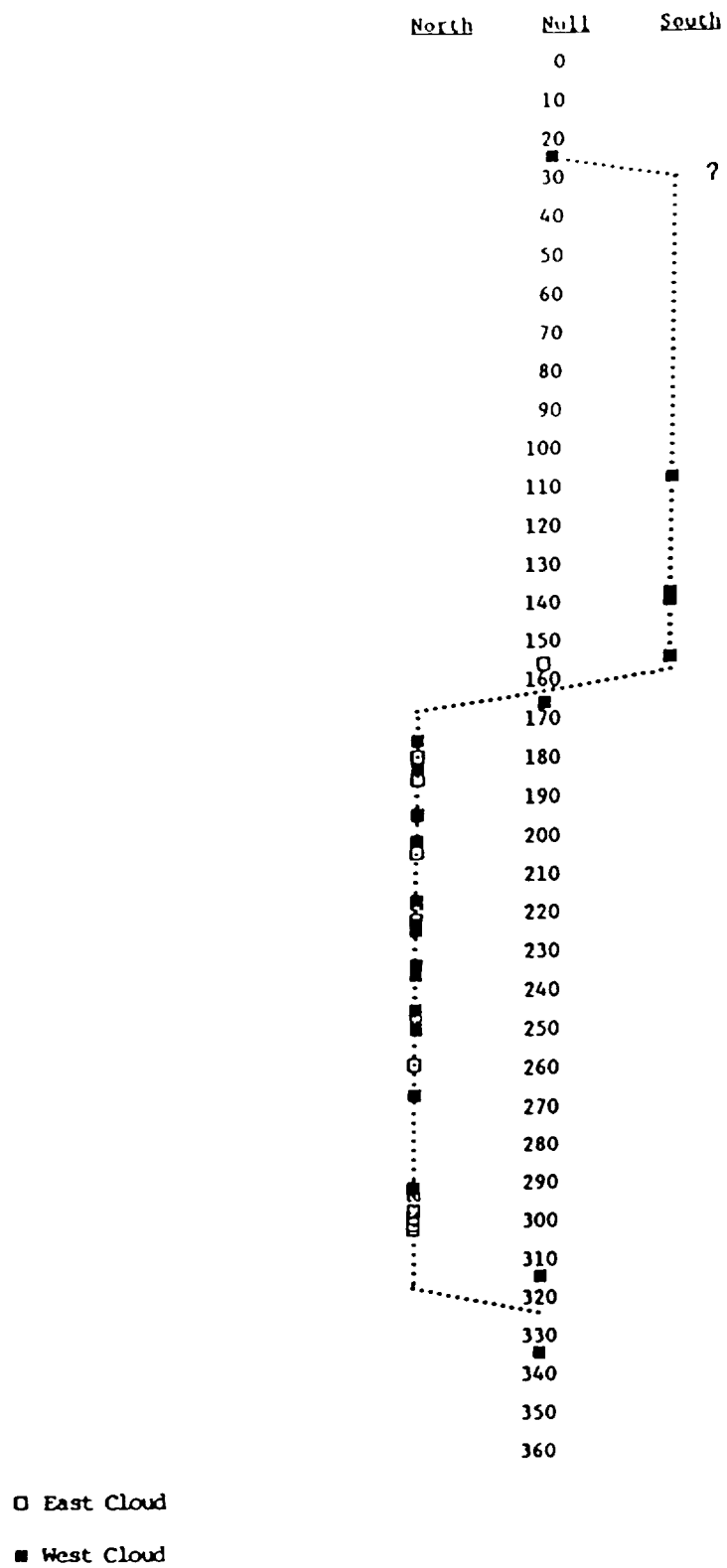


Figure 4

IO SODIUM CLOUD 1981

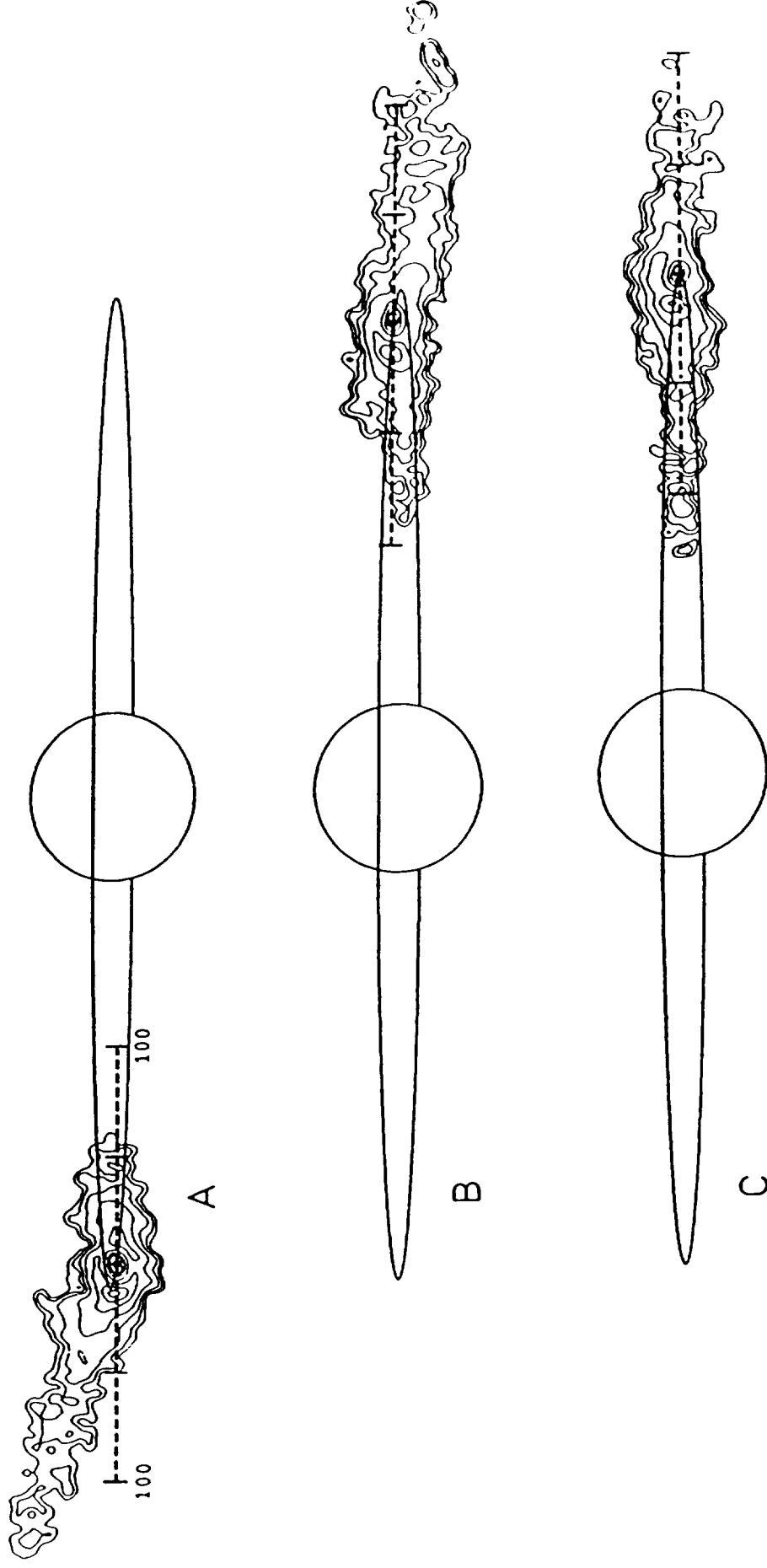
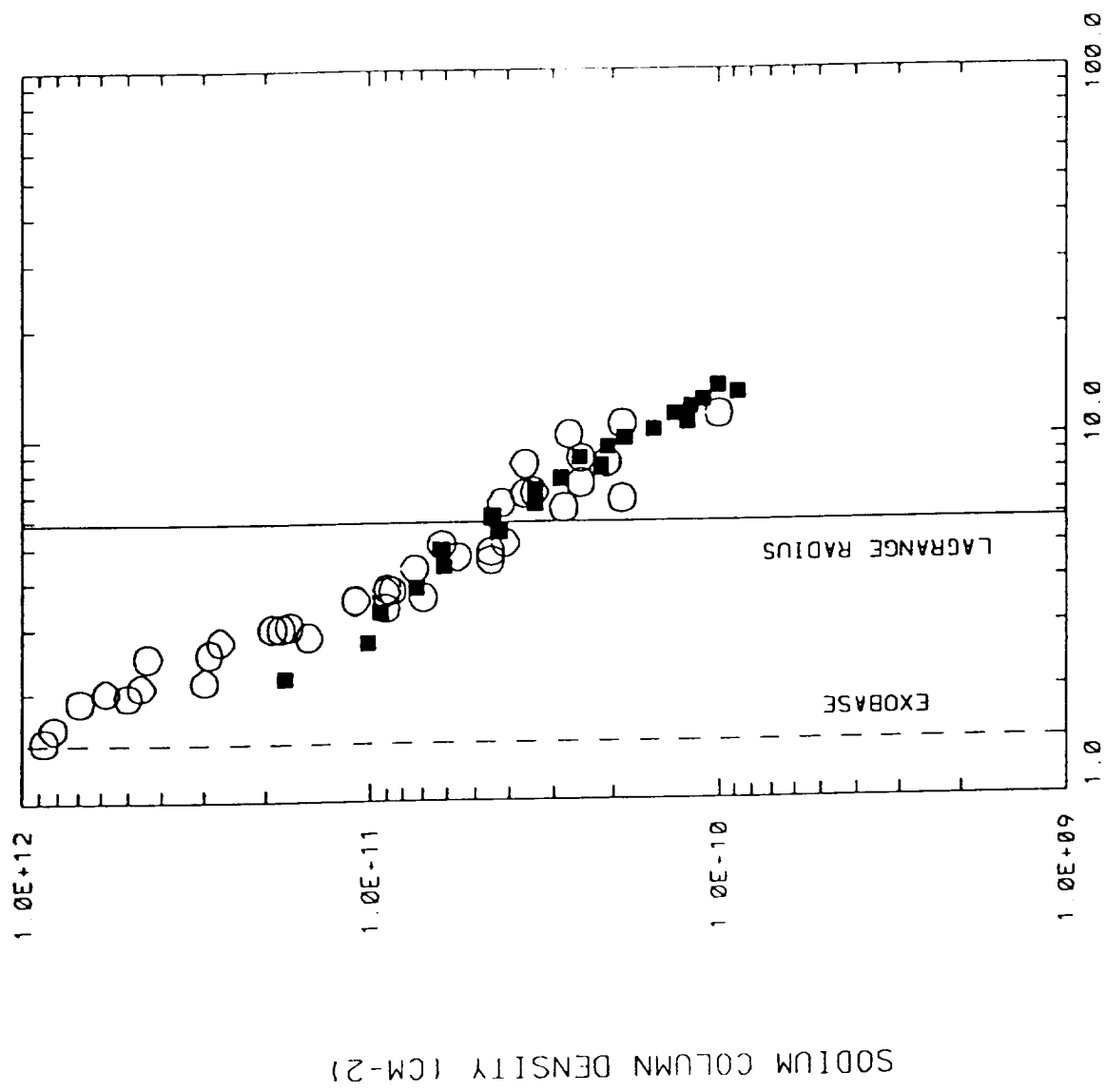
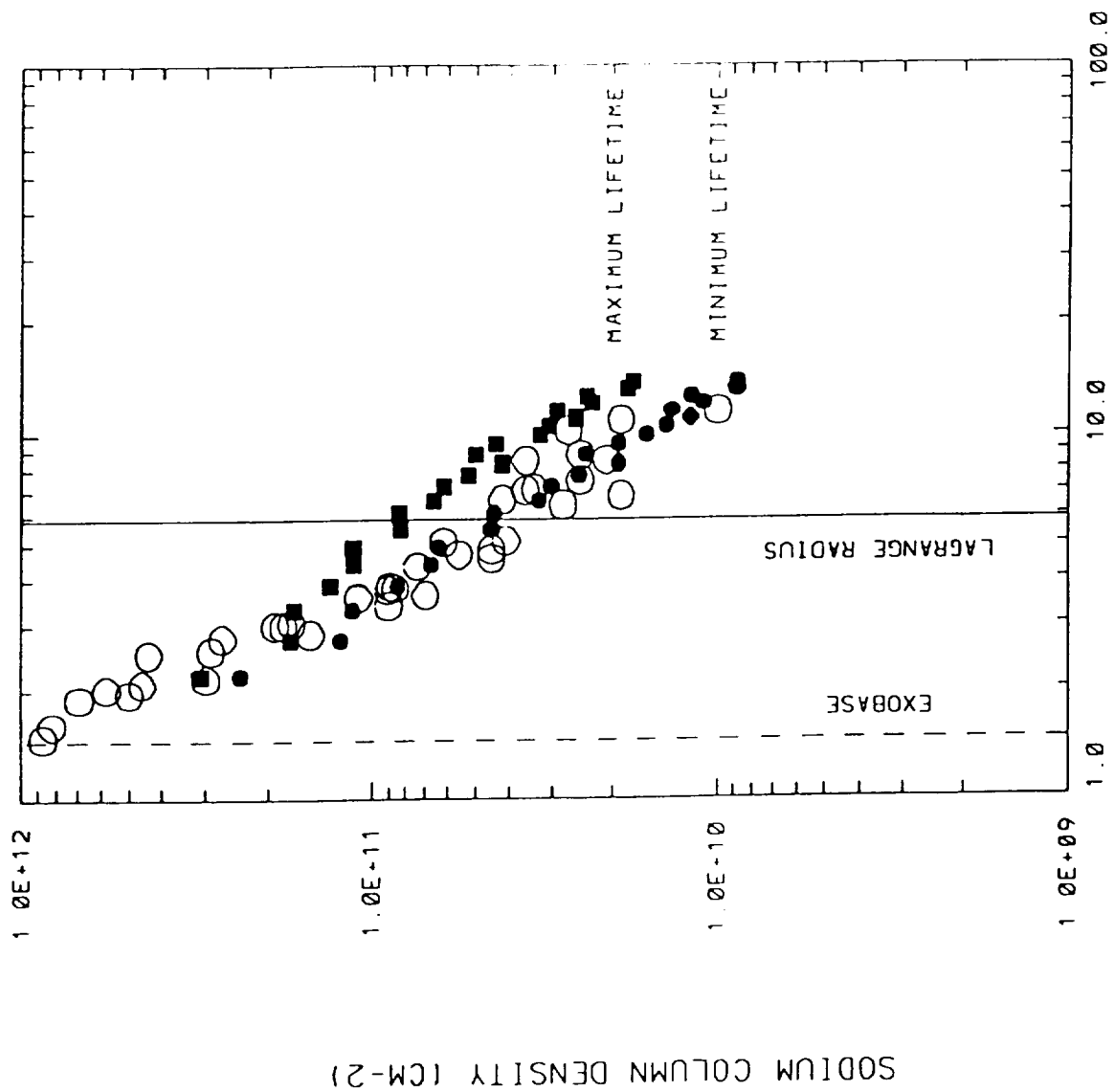


Figure 5



DISTANCE FROM THE CENTER OF IO (10 RADII)



DISTANCE FROM THE CENTER OF IO (IO RADII)

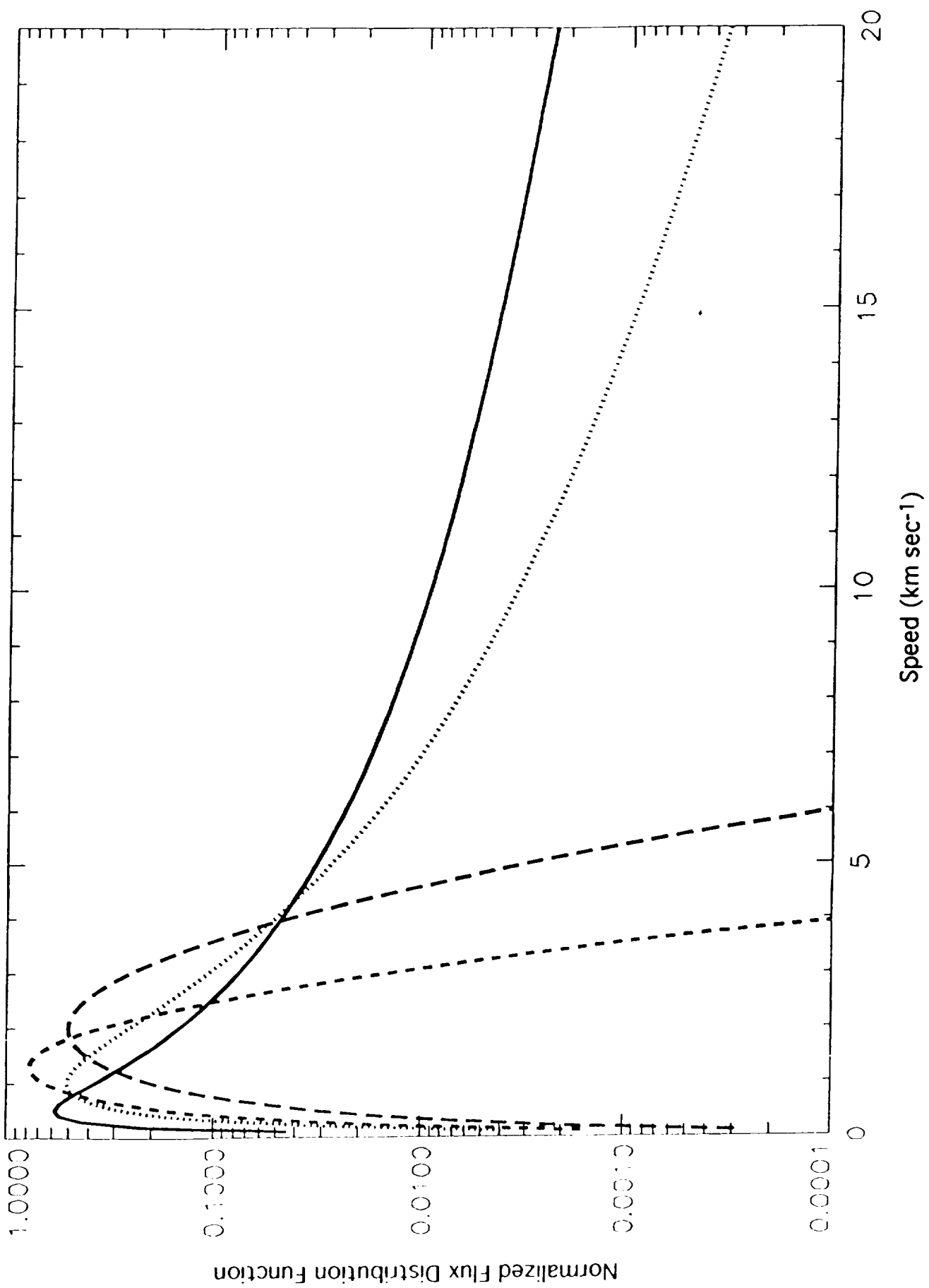
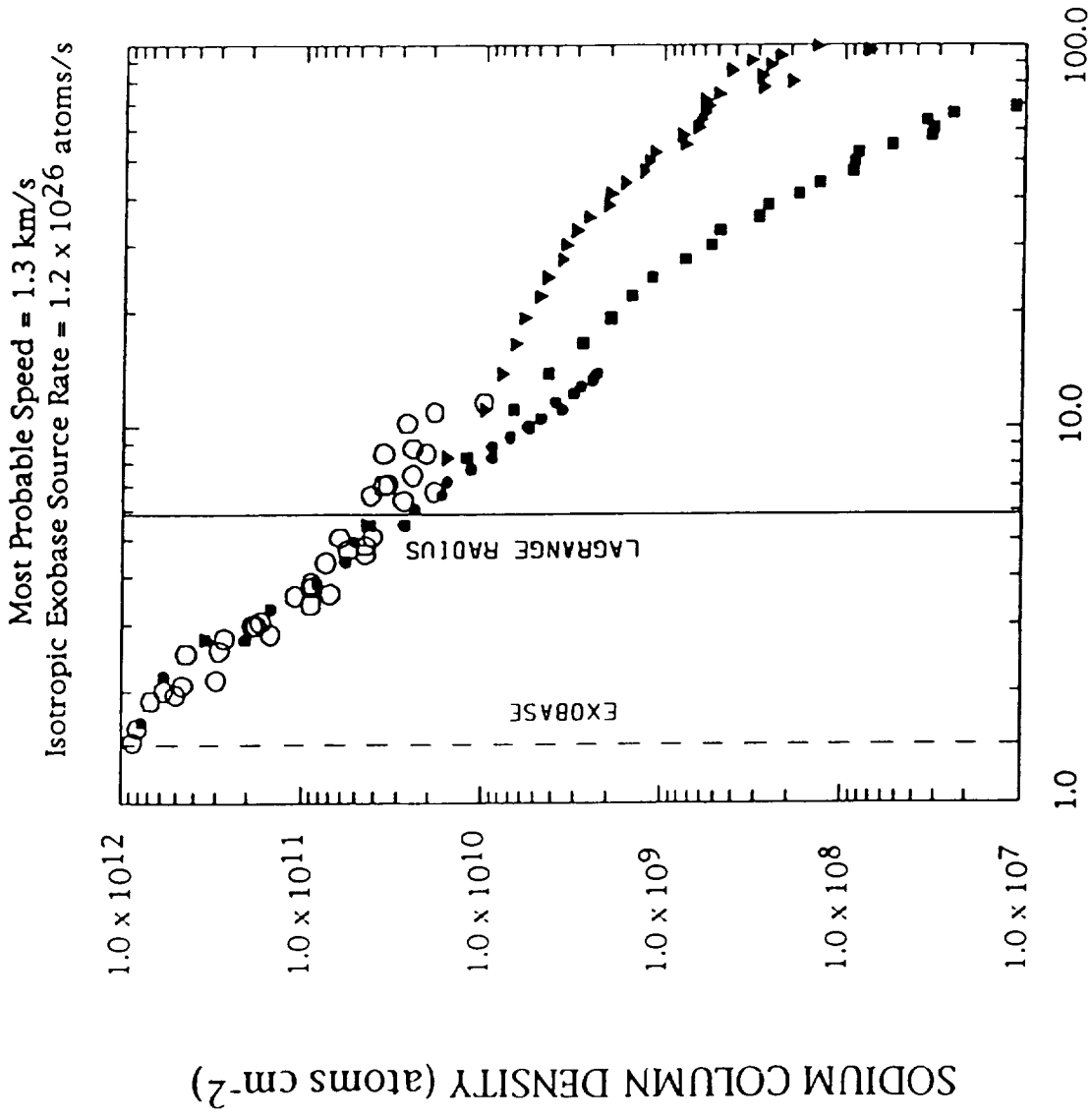


Figure 8

ECLIPSE DATA

Maxwell-Boltzmann Flux Distribution



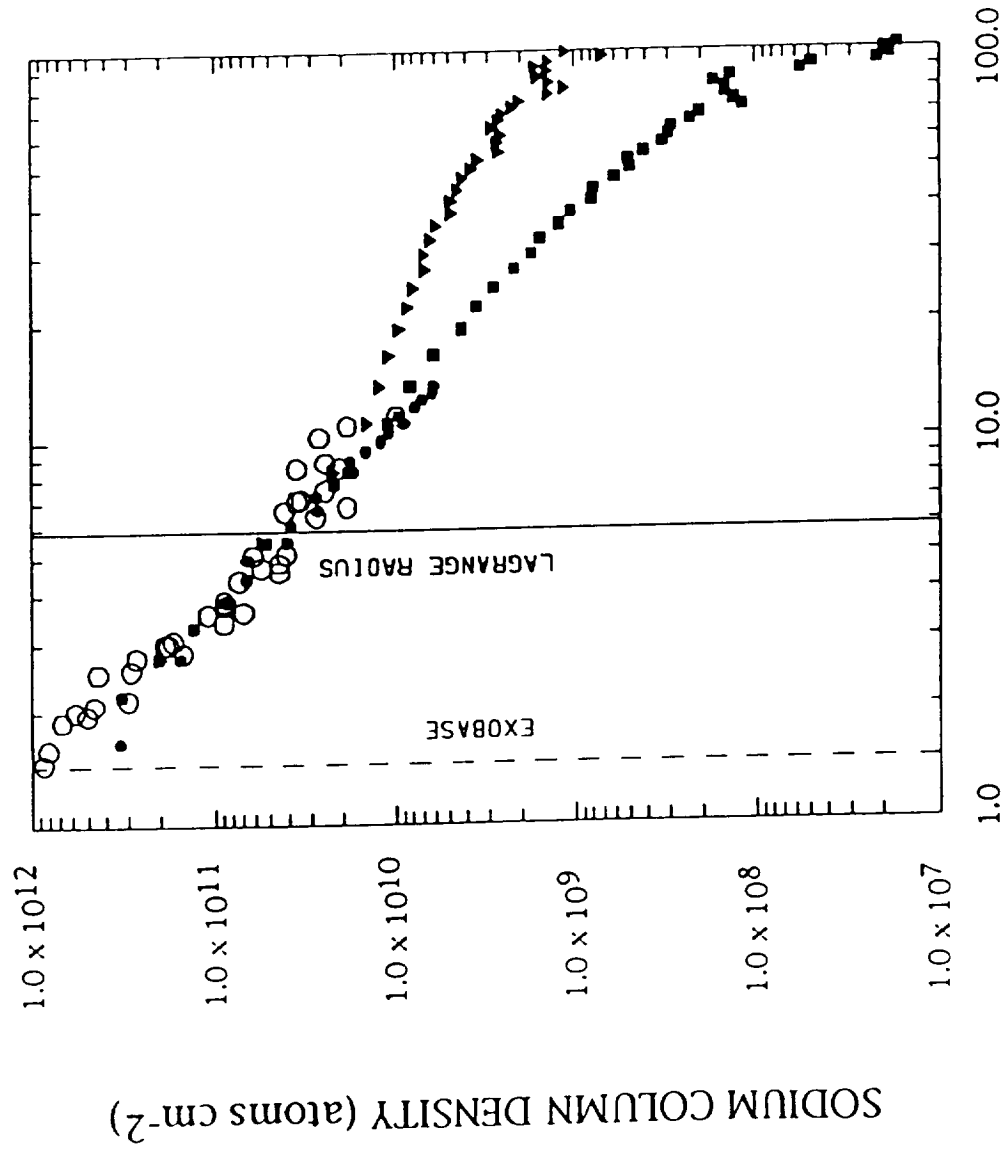
RADIAL DISTANCE FROM IO (R_{IO})

Figure 9a

ECLIPSE DATA

Maxwell-Boltzmann Flux Distribution

Most Probable Speed = 2.0 km/s
Isotropic Exobase Source Rate = 0.75×10^{26} atoms/s



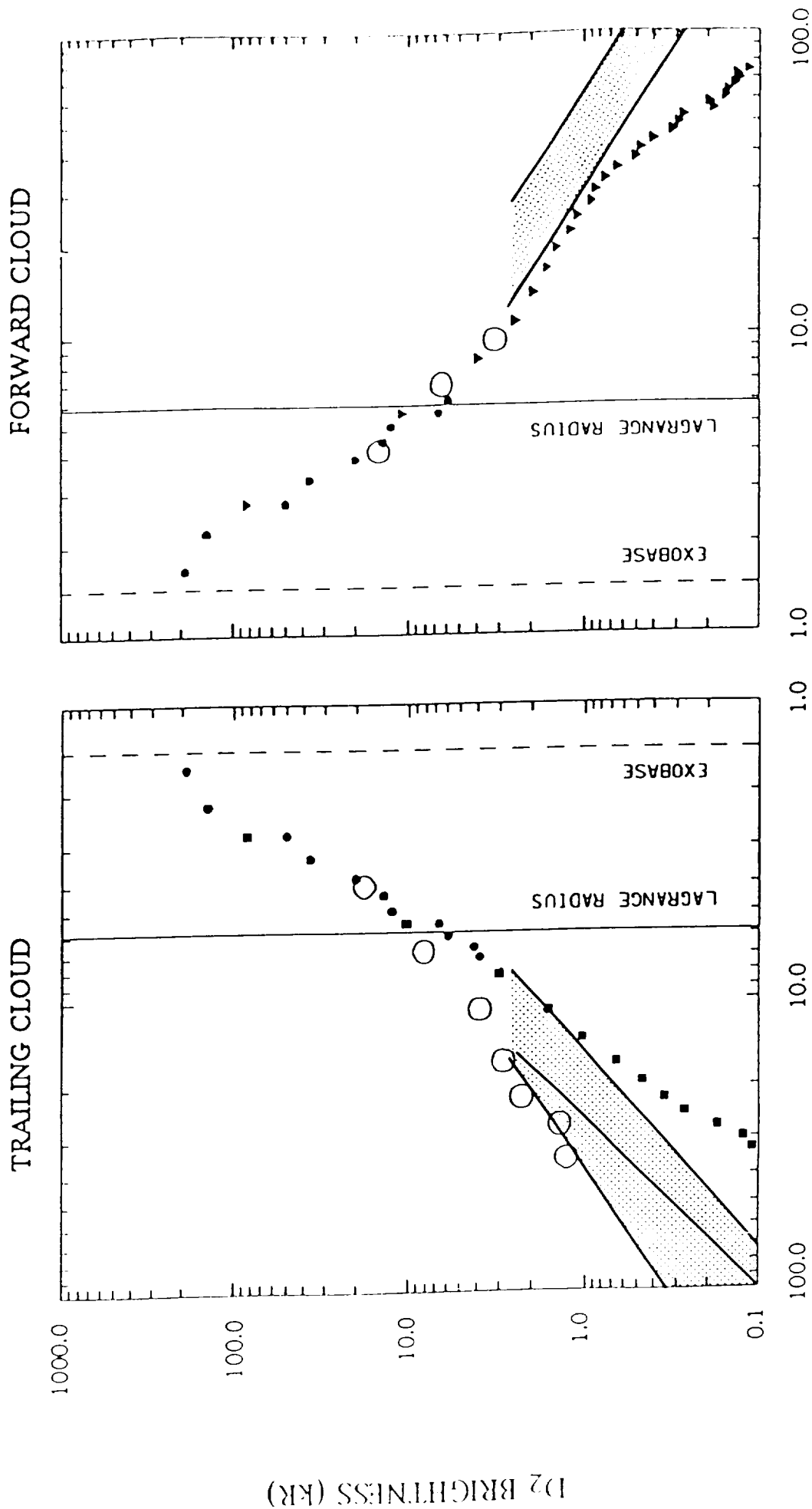
RADIAL DISTANCE FROM IO (R_{IO})

EMISSION DATA

Maxwell-Boltzmann Flux Distribution

Most Probable Speed = 1.3 km/s

Isotropic Exobase Source Rate = 1.2×10^{26} atoms/s



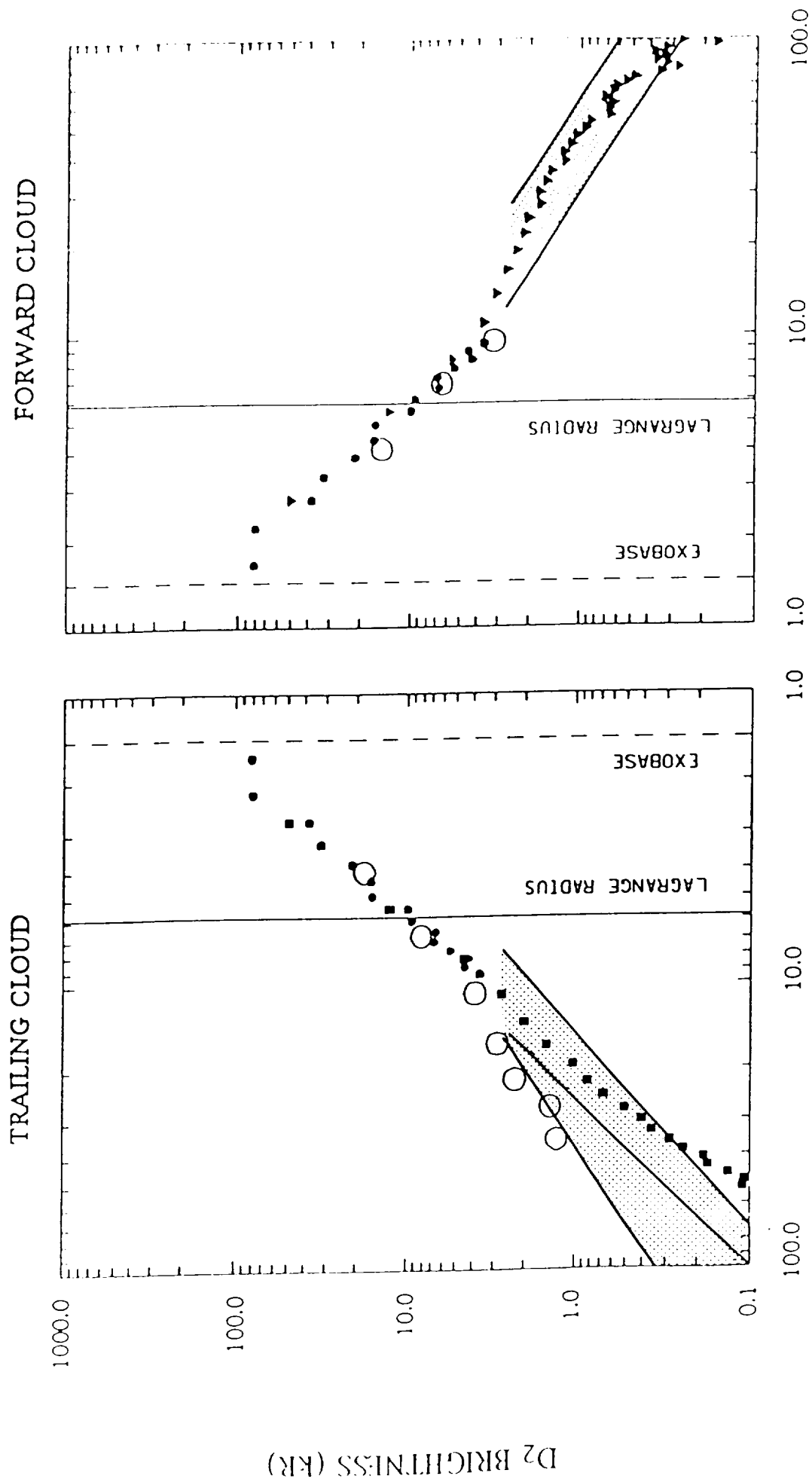
RADIAL DISTANCE FROM IO (R₁₀)

Figure 10a

EMISSION DATA

Maxwell-Boltzmann Flux Distribution

Most Probable Speed = 2.0 km/s
Isotropic Exobase Source Rate = 0.75×10^{26} atoms/s

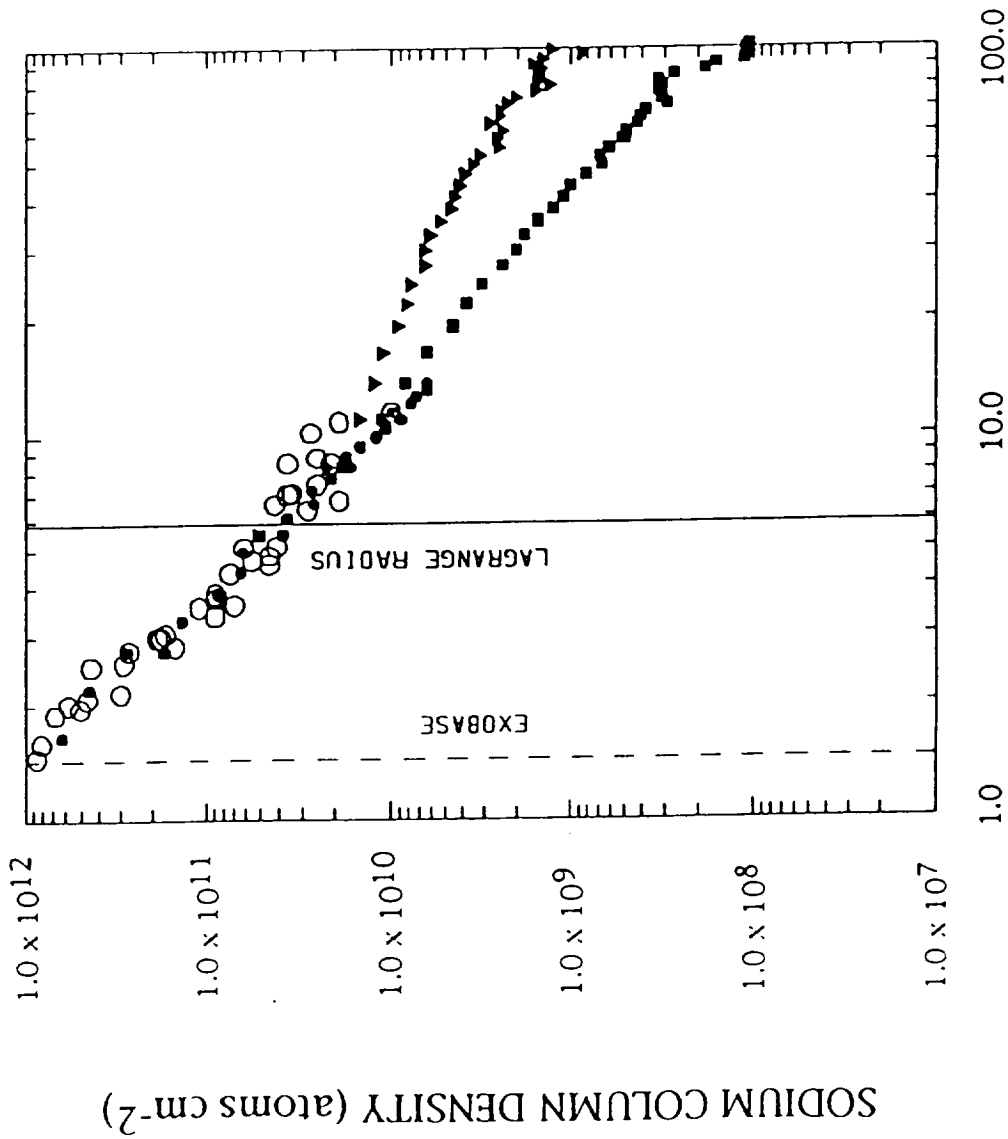


RADIAL DISTANCE FROM IO (R_{IO})

ECLIPSE DATA

Classical Sputtering Flux Distribution

Most Probable Speed = 1.0 km/s
Velocity Dispersion: $\alpha = 3.0$
Isotropic Exobase Source Rate = 1.3×10^{26} atoms/s

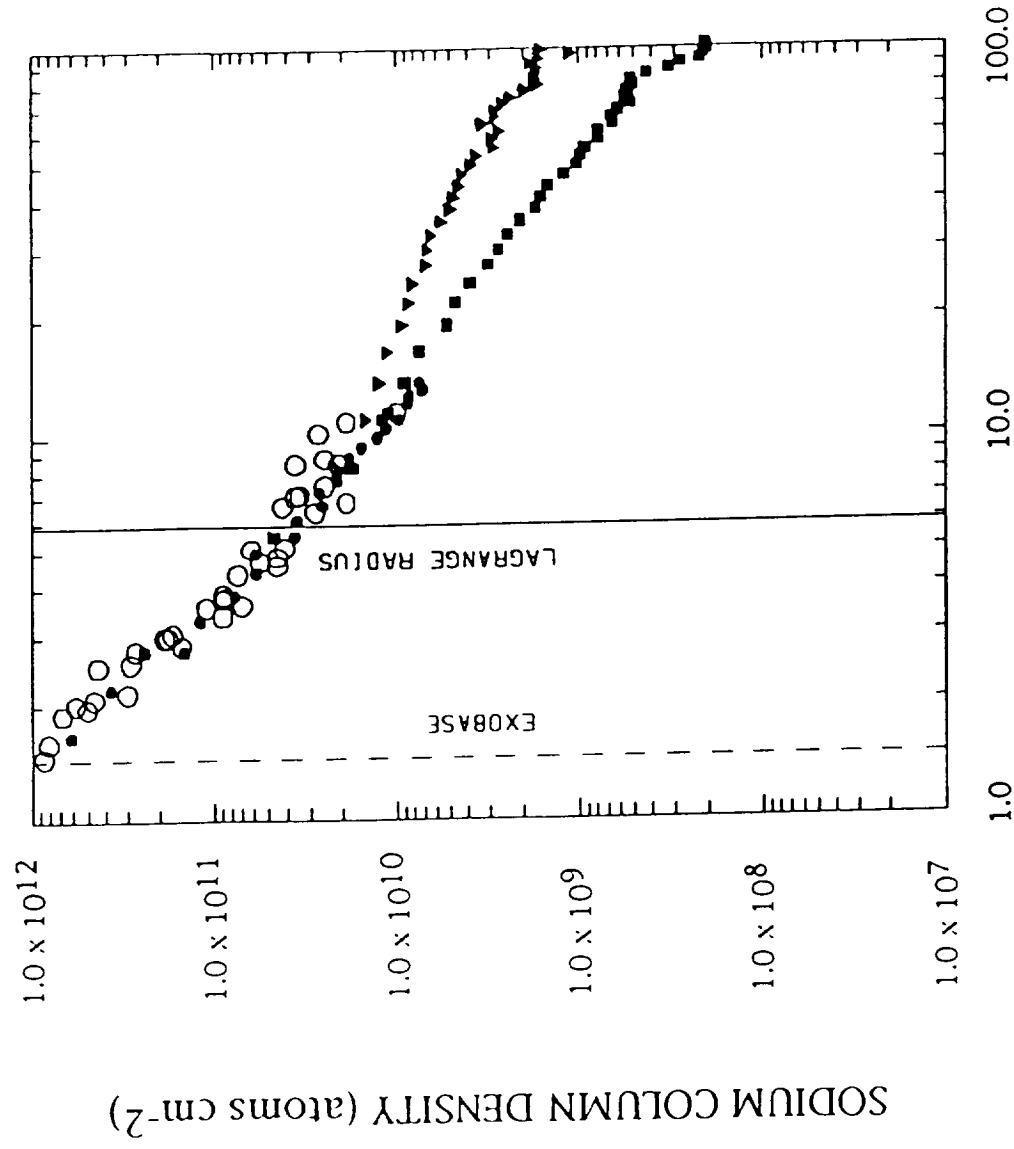


RADIAL DISTANCE FROM IO (R_{IO})

ECLIPSE DATA

Modified Sputtering Flux Distribution

Most Probable Speed = 0.5 km/s
Velocity Dispersion : $\alpha = 7/3$
Isotropic Exobase Source Rate = 1.7×10^{26} atoms/s



RADIAL DISTANCE FROM IO (R_{IO})

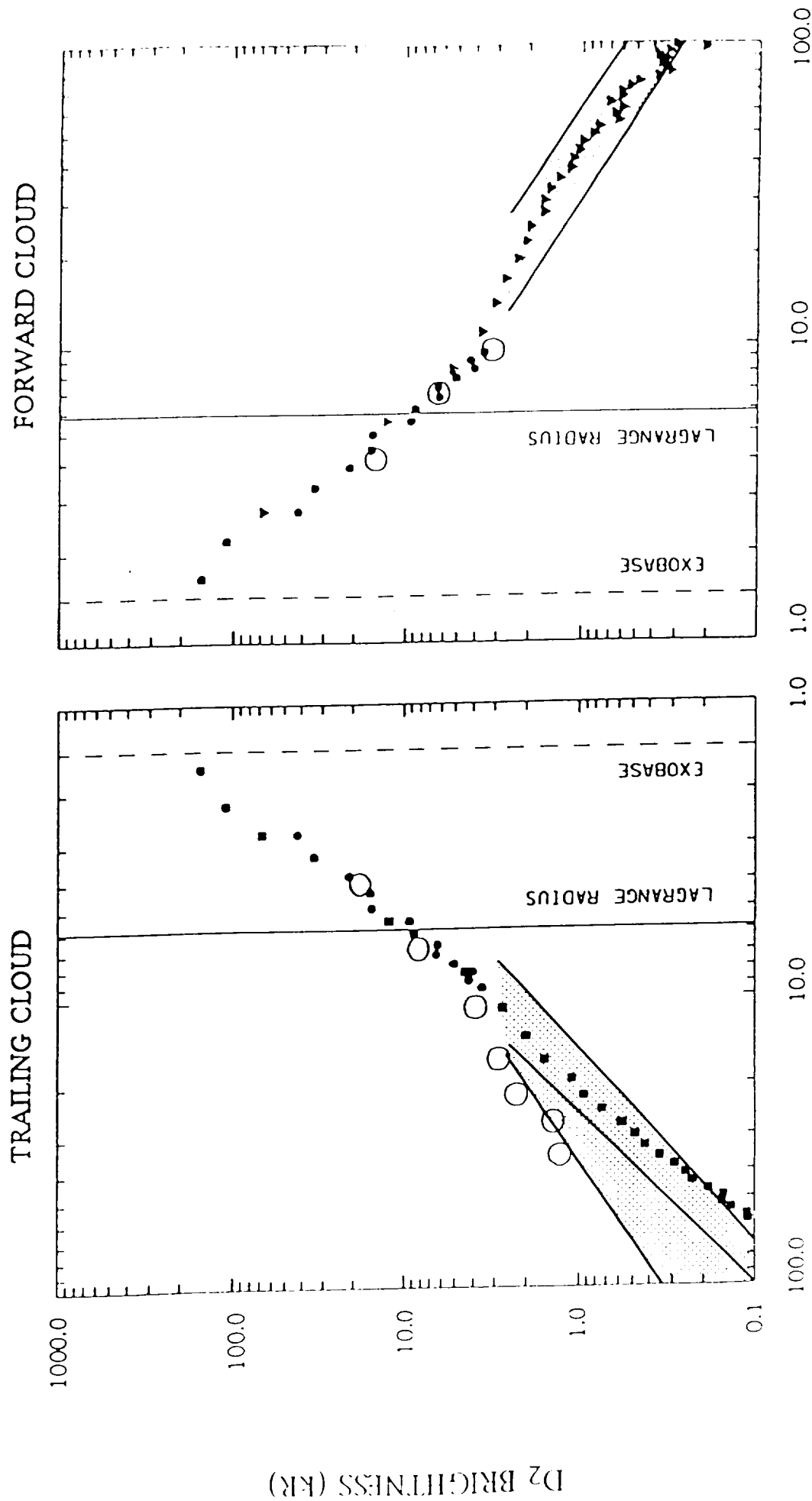
EMISSION DATA

Classical Sputtering Flux Distribution

Most Probable Speed = 1.0 km/s

Velocity Dispersion : $\alpha = 3.0$

Isotropic Exobase Source Rate = 1.3×10^{26} atoms/s



RADIAL DISTANCE FROM IO (R_{IO})

EMISSION DATA

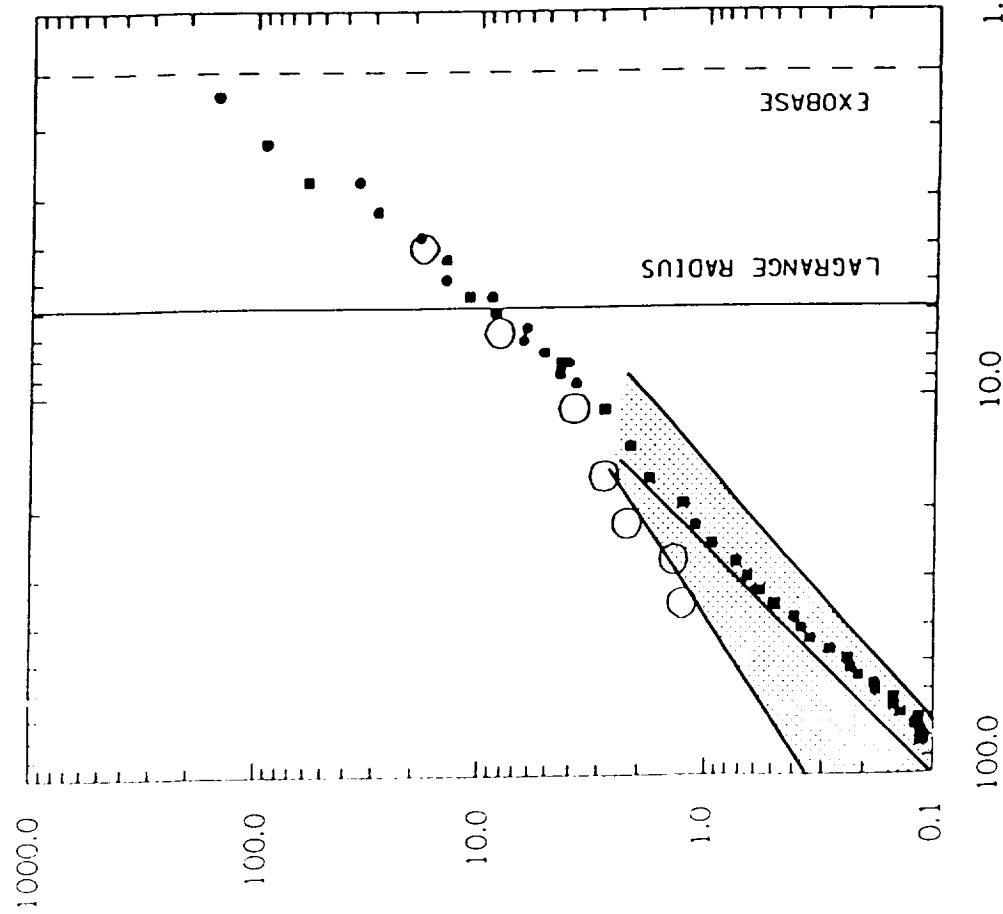
Modified Sputtering Flux Distribution

Most Probable Speed = 0.5 km/s

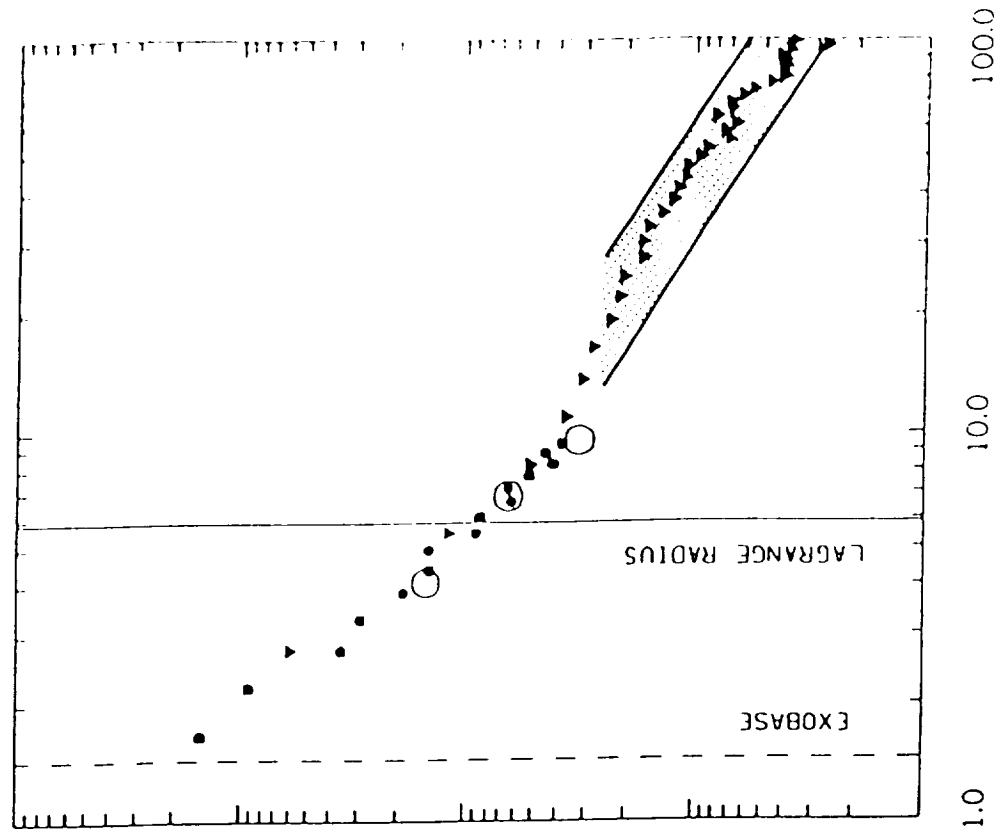
Velocity Dispersion : $\alpha = 7/3$

Isotropic Exobase Source Rate = 1.7×10^{26} atoms/s

TRAILING CLOUD



FORWARD CLOUD

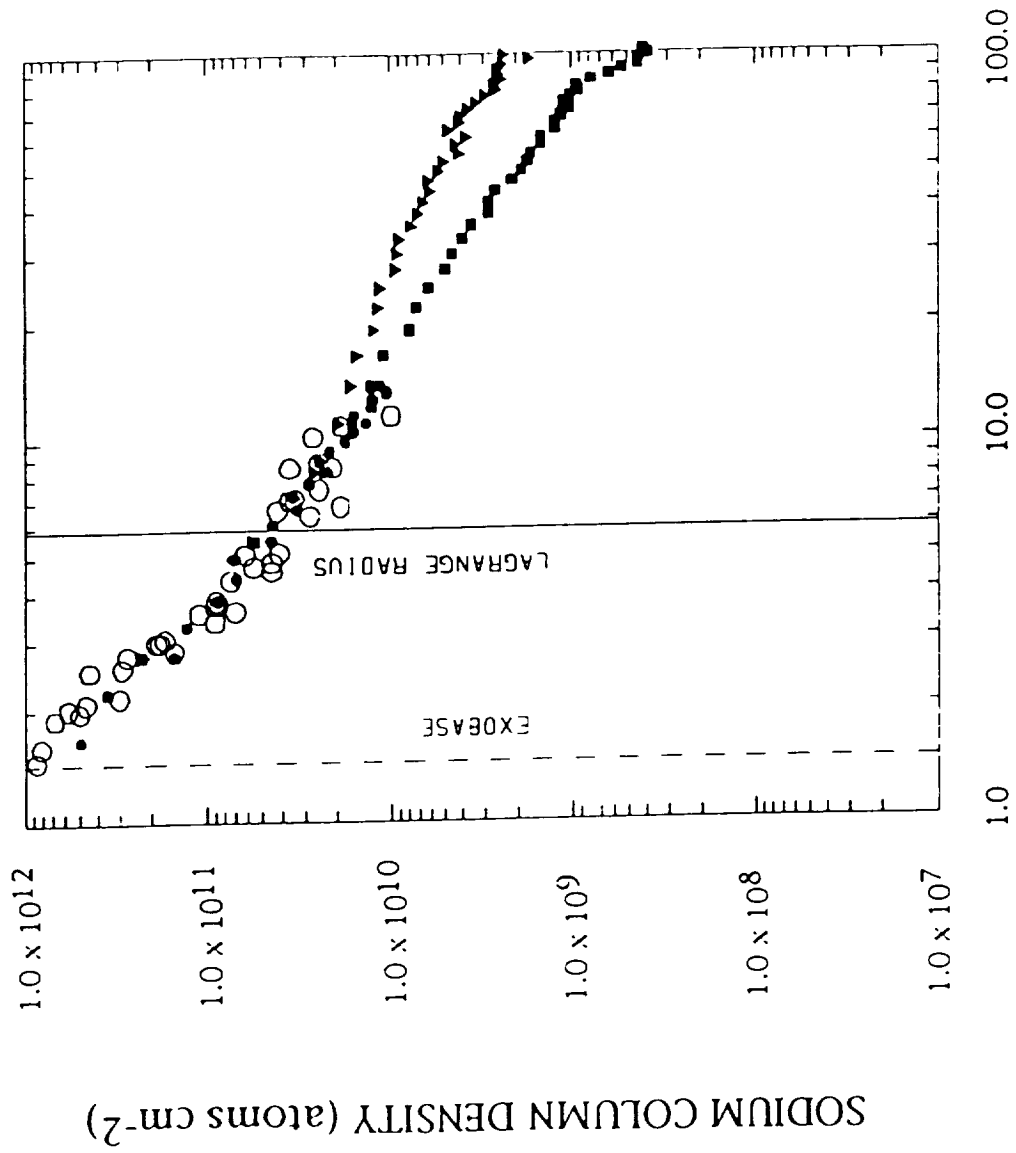


RADIAL DISTANCE FROM IO (R_{10})

ECLIPSE DATA

Modified Sputtering Flux Distribution

Most Probable Speed = 0.4 km/s
 Velocity Dispersion : $\alpha = 2$
 Isotropic Exobase Source Rate = 1.9×10^{26} atoms/s



RADIAL DISTANCE FROM IO (R_{IO})

EMISSION DATA

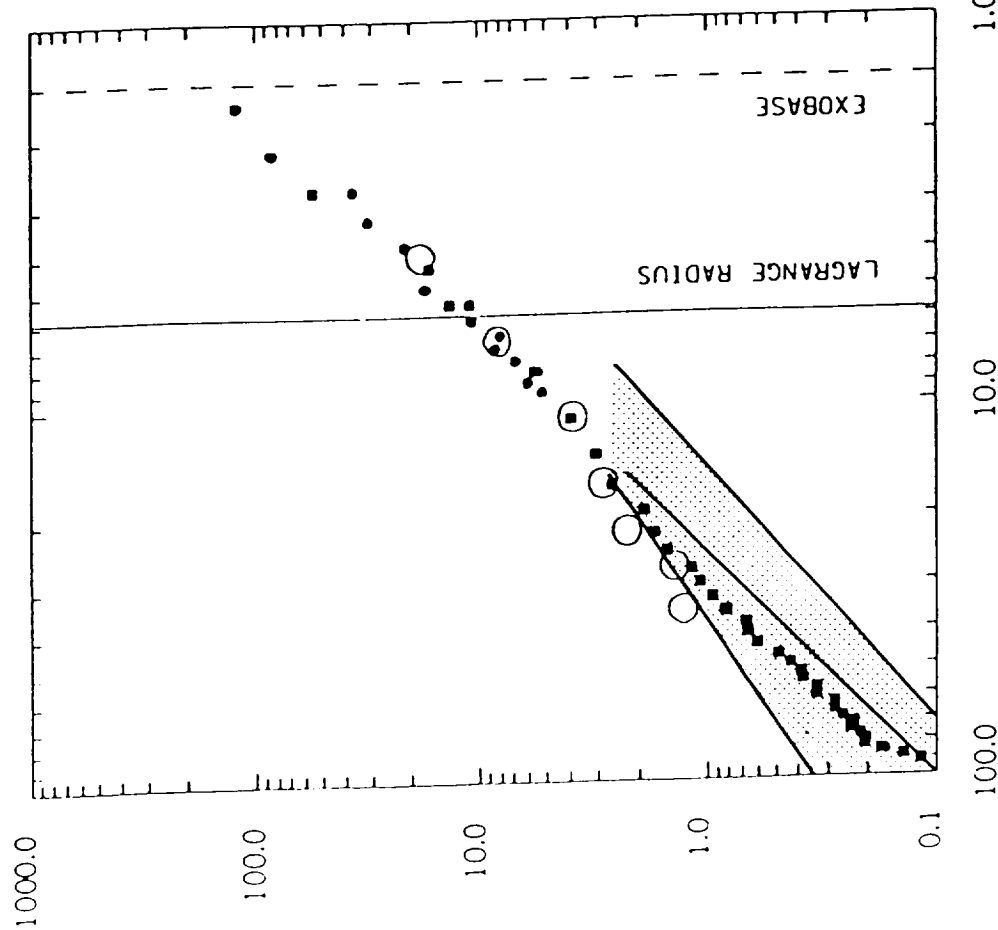
Modified Sputtering Flux Distribution

Most Probable Speed = 0.4 km/s

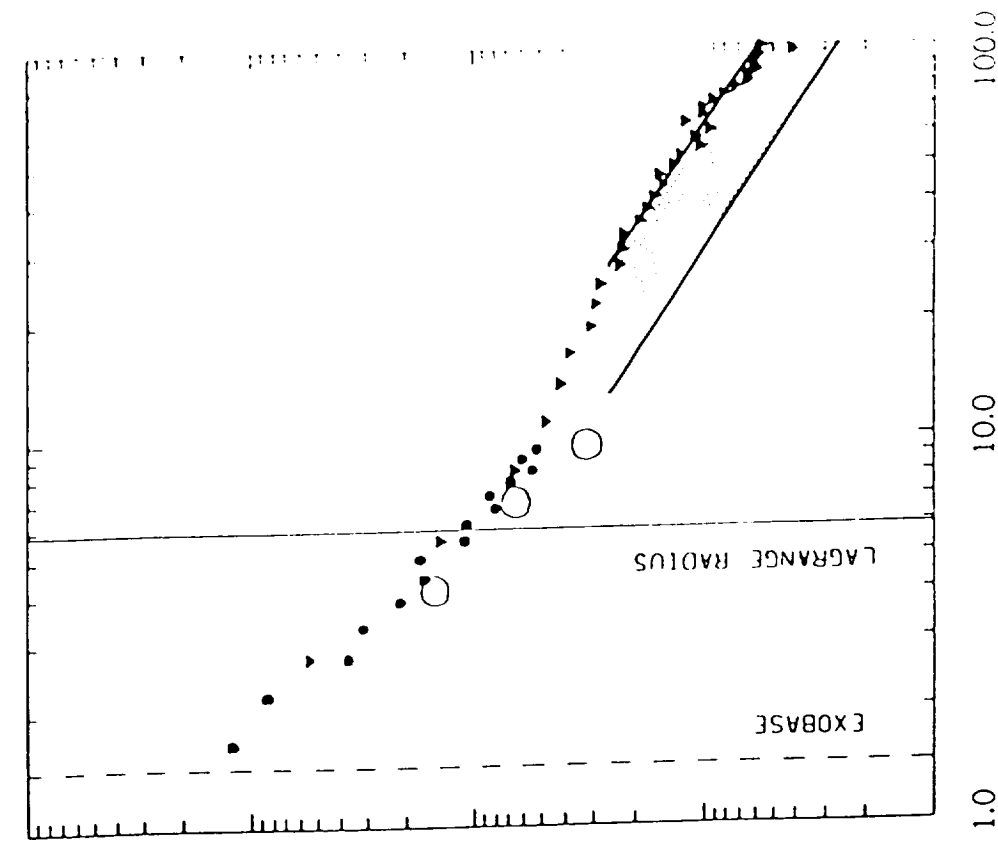
Velocity Dispersion : $\alpha = 2$

Isotropic Exobase Source Rate = 1.9×10^{26} atoms/s

TRAILING CLOUD



FORWARD CLOUD



RADIAL DISTANCE FROM IO (R_{IO})

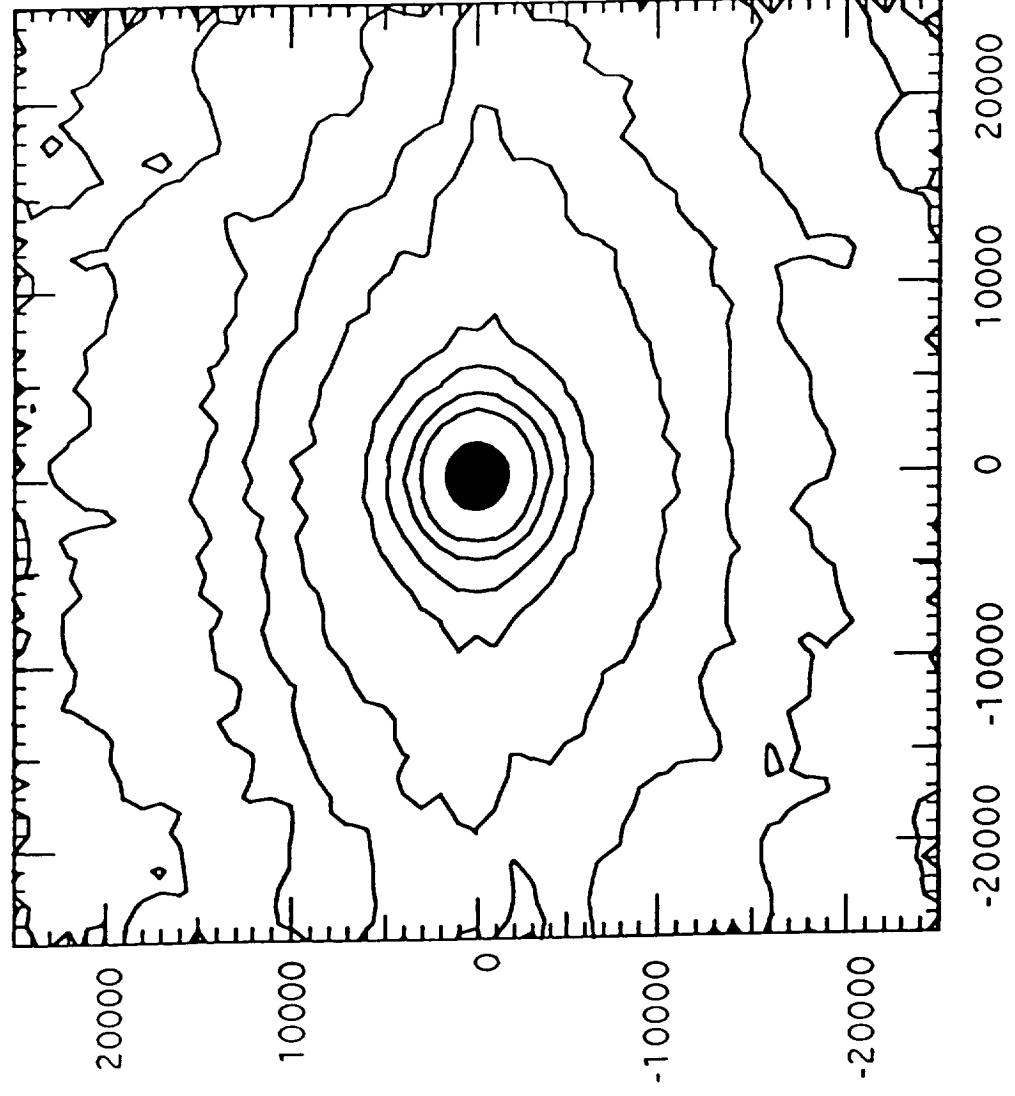


Figure 15

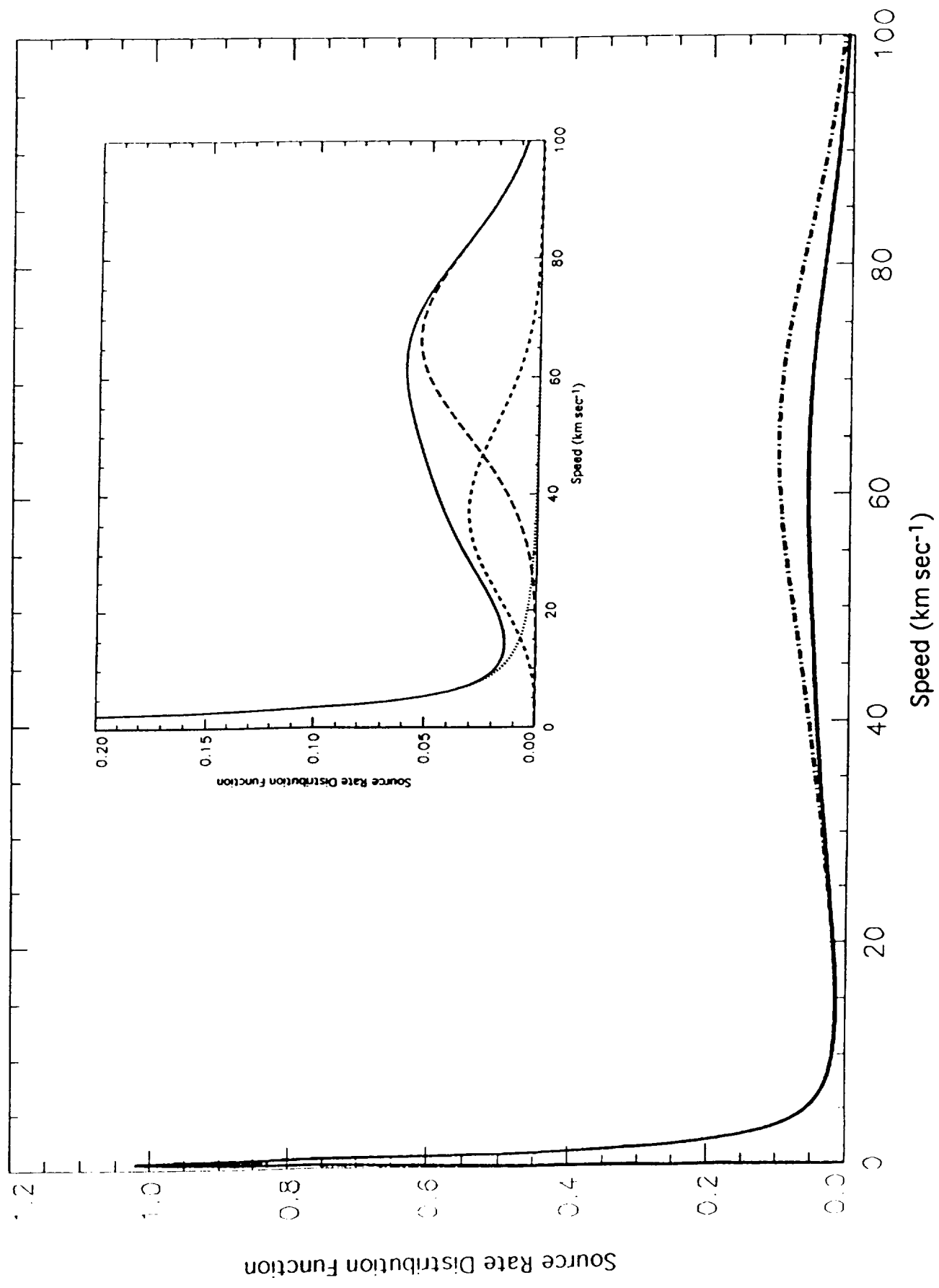


Figure 16